MDSC-mediated metabolic competition drives T cell senescence via the AMPK-Foxo1 and PPP-redox axes

Qiyao Pu[1,2,3,4#], Jiangyan Yuan[2,3,4#], Meng Zhao[1,2,3,4], Meiqing Jiang[1,2,3,4], Xinyue Wang[1,2,3,4], Yajun Leng[2,3,4], Zhiyun Yang[4,6*], Yaxian Kong[1,2,3,4,5*]

[1]*Peking University Ditan Teaching Hospital, National Key Laboratory of Intelligent Tracking and Forecasting for Infectious Diseases, Beijing Ditan Hospital, Beijing 100015, China*

[2]*Beijing Institute of Infectious Diseases, Beijing, 100015, China*

[3]*Beijing Key Laboratory of Viral Infectious Diseases, Beijing Ditan Hospital, Capital Medical University, Beijing 100015, China*

[4]*National Center for Infectious Diseases, Beijing Ditan Hospital, Capital Medical University, Beijing 100015, China*

[5]*Clinical Center for HIV/AIDS, Beijing Ditan Hospital, Capital Medical University, Beijing 100015, China*

[6]*Center of Integrative Medicine, Beijing Ditan Hospital, Capital Medical University, Beijing, 100015, China*

#These authors contributed equally to this work

*Correspondence to:

Yaxian Kong, Ph.D.,

National Key Laboratory of Intelligent Tracking and Forecasting for Infectious Diseases,

Beijing Ditan Hospital, Capital Medical University,

Beijing 100015, China

Email: kongyaxian@ccmu.edu.cn

Zhiyun Yang, M.D., Ph.D.

Center of Integrative Medicine,

Beijing Ditan Hospital, Capital Medical University,

Beijing, 100015, China

Email: yangzhiyun2016@163.com

The authors have declared that no conflict of interest exists.

35

Abstract

T cell senescence represents a state of functional dysregulation that compromises host immunity in tumors and severe infections. While myeloid-derived suppressor cells (MDSCs) are established drivers of immunosuppression, their role in T cell senescence remains poorly defined. Here, we identify MDSC-mediated glucose deprivation and subsequent metabolic reprogramming as an important mechanism promoting T cell senescence. MDSCs exhibit hyper-glycolytic activity via the upregulation of glucose transporter 1 (GLUT1) and hexokinase 2 (HK2), creating a glucose-deprived microenvironment that imposes dual energy and oxidative stress on T cells. Mechanistically, ATP depletion induced by glucose starvation activates the AMPK-Foxo1 signaling axis, promoting Foxo1 nuclear translocation and p16-mediated cell-cycle arrest. Meanwhile, restricted glucose flux through the pentose phosphate pathway (PPP) depletes NADPH and glutathione (GSH) pools, triggering cumulative DNA damage and mitochondrial dysfunction. These senescent T cells exhibit classical senescence-associated-β-galactosidase (SA-β-gal) activity and a senescence-associated secretory phenotype (SASP) that further destabilizes the immune landscape. Importantly, pharmacological inhibition of MDSCs glycolysis or restoration of T cell redox homeostasis effectively bypasses the senescence program. *In vivo*, systemic interventions modulating this metabolic and signaling pathway alleviate T cell senescence, significantly improving survival in the cecal ligation and puncture (CLP) model and suppressing tumor progression in the B16F10 melanoma model. Our study reveals MDSC-driven metabolic competition as a checkpoint in T cell senescence, highlighting the AMPK-Foxo1 and PPP-redox axes as potent therapeutic targets to restore immune function in diverse disease contexts.

Keywords: Myeloid-derived suppressor cells; T cell senescence; Metabolic competition; AMPK-Foxo1 axis; PPP-redox axis

Introduction

As the central orchestrators of adaptive immunity, T cells are indispensable for surveilling malignant transformation and clearing pathogenic invasions [1]. Specifically, in severe systemic infections such as sepsis, robust T cell responses are critical for infection control, whereas their functional impairment directly precipitates lethal immune paralysis [2]. Similarly, in immunogenic solid tumors, T cells dictate the magnitude of anti-tumor immunity and the ultimate response to immune checkpoint blockade [3]. Under pathological conditions characterized by persistent antigen exposure or excessive inflammation, T cells may develop a state of functional dysregulation known as cellular senescence [4-6]. This state is characterized by cell-cycle arrest and impaired effector function, along with a distinct molecular signature comprising progressive telomere attrition, cumulative DNA damage, severe mitochondrial dysfunction and global remodeling of the epigenetic landscape [7-9]. Crucially, senescent T cells not only lose their cytotoxic potential against tumors or pathogens but also acquire a senescence-associated secretory phenotype (SASP) that releases proinflammatory cytokines, chemokines, growth factors and matrix metalloproteinases [4, 10]. This secretory profile remodels the immune microenvironment and disrupts tissue homeostasis through paracrine mechanisms that exacerbate tissue injury and compromise immune surveillance [11]. Clinical evidence increasingly indicates that the accumulation of these senescent populations correlates with poor prognosis in malignancies [12, 13]. While its precise pathogenic role in sepsis is an emerging field, recent evidence suggests it may also contribute to adverse outcomes during severe infections, as targeting IL-33-induced T cell senescence effectively improves survival in septic models [2, 14]. These findings underscore the necessity to elucidate the mechanisms governing T cell senescence across diverse disease contexts.

Recent breakthroughs in immunometabolism have established metabolic reprogramming as a fundamental checkpoint that determines T cell differentiation, function, and long-term survival [15, 16]. The transition of T cells from a quiescent state to an activated effector phenotype necessitates a rapid metabolic switch from oxidative phosphorylation to aerobic glycolysis and glutaminolysis, which supports the bioenergetic and biosynthetic demands of clonal expansion and effector molecule synthesis [15, 17-19]. This intense reliance on exogenous nutrients renders effector T cells acutely vulnerable within resource-constrained microenvironments where they must compete for limited metabolic substrates. In the highly competitive ecological niche of the tumor microenvironment, tumor cells and regulatory immune subsets exert severe metabolic pressure on effector T cells by monopolizing critical nutrients [20, 21]. It has been demonstrated that regulatory T cells (Tregs) can starve effector T cells of glucose and

subsequently trigger the p38 MAPK signaling cascade to induce a DNA damage response (DDR) that promotes T cell senescence [22]. Furthermore, tumor cells exploit their aberrant glycolytic flux and amino acid uptake to further deplete the nutrient pool while simultaneously triggering metabolic stress, which activates cAMP and MAPK signaling pathways that accelerate senescence [23, 24]. These findings have established a clear link between metabolic stress and immunosenescence.

Although the paradigm of metabolic competition inducing T cell senescence is well elucidated in tumor models, its relevance in severe infections such as sepsis remains poorly understood [22, 25, 26]. The pathology of sepsis typically manifests as a biphasic process evolving from an initial hyperinflammatory phase to a protracted state of immune paralysis characterized by extensive lymphocyte apoptosis, T cell anergy and susceptibility to secondary infections [27, 28]. While Treg expansion is not always the predominant feature of this immunosuppressive phase, myeloid-derived suppressor cells (MDSCs) represent another critical immunoregulatory population that accumulates extensively during sepsis, acting as a central driver of sepsis-induced immunoparalysis. These cells exert potent suppression via mechanisms including arginase-1 (Arg1) and inducible nitric oxide synthase (iNOS) activity, PD-L1 expression, and the secretion of suppressive cytokines such as IL-10 and TGF-β [29]. Notably, these myeloid cells possess metabolic plasticity involving enhanced glycolysis and fatty acid oxidation, which may confer a competitive advantage in nutrient-deprived environments [20, 30, 31]. It remains to be determined whether MDSCs utilize this metabolic capacity to deprive neighboring T cells of glucose or other key nutrients, actively driving them into senescence. Elucidating whether this metabolic competition represents a shared mechanism across diverse pathologies ranging from neoplasia to sepsis would help provide a broader theoretical framework for immunosenescence.

In this study, we aimed to systematically investigate whether MDSCs induce T cell senescence through a mechanism of metabolic deprivation and to delineate the downstream signaling networks involved. We demonstrate that in CLP mice and in the B16F10 and MC38 tumor models, MDSCs exhibit a high capacity for glucose uptake and glycolysis, which severely restrict glucose availability in the microenvironment. This metabolic stress activates the AMPK-Foxo1 axis in T cells and upregulates cell-cycle inhibitors, thereby promoting a stable senescence program under the tested conditions in this study. We further reveal that glucose restriction impairs the pentose phosphate pathway (PPP), reducing NADPH and glutathione production, which triggers immunosenescence associated with DNA damage and mitochondrial dysfunction. Our *in vivo* studies demonstrate that systemic interventions modulating these

pathways effectively alleviate T cell senescence and improves survival in CLP model while suppressing tumor progression in the B16F10 melanoma model. These findings identify MDSC-driven metabolic competition as a critical mechanism of T cell senescence and suggest a novel therapeutic target for restoring T cell function.

Materials and Methods

Clinical specimens.

Fourteen patients with sepsis diagnosed according to the Third International Consensus Definitions for Sepsis and Septic Shock (Sepsis-3) [32], six patients with hepatocellular carcinoma (HCC) diagnosed according to the American Association for the Study of Liver Diseases (AASLD) or European Association for the Study of the Liver (EASL) criteria [33, 34], and eleven healthy controls (HC) without known acute infection, malignancy, or other major clinical diseases were enrolled. The study was approved by the Ethics Committee of Beijing Ditan Hospital, Capital Medical University (DTEC-KY2026-038-02 for the sepsis cohort and DTEC-KY2023-014-01 for the HCC and healthy-control cohorts), and written informed consent was obtained from all participants before enrollment. Healthy controls were age- and sex-matched to the patient cohorts. The demographic and clinical characteristics of all three cohorts are summarized in Supplementary Table 1.

Animals

This study used male and female C57BL/6 mice aged 6-8 weeks (Jiangsu Jicui Yao Kang Biotechnology Co., Ltd., China). Male mice were used for the CLP sepsis experiments, whereas female mice were used for the B16F10 tumor experiments. Mice were housed in the Laboratory Animal Center of Capital Medical University (AAALAC-accredited) under specific pathogen-free (SPF) conditions, with a 12-h light/12-h dark cycle and ad libitum access to autoclaved water and irradiated standard chow. No more than five mice were housed per cage. All animal experiments were approved by the Animal Ethics Committee of Capital Medical University (AEEI-2025-267) and conducted in accordance with the Guidelines for the Care and Use of Laboratory Animals.

Sepsis in male C57BL/6 mice was induced by cecal ligation and puncture (CLP) surgery. Sham-operated mice underwent laparotomy with cecal exposure but without ligation or puncture. B16F10 melanoma cells were cultured in RPMI 1640 medium (Gibco) supplemented with 10% fetal bovine serum (FBS; Gibco) and 1× penicillin–streptomycin (Gibco), whereas MC38 cells were cultured in DMEM (Gibco) supplemented with 10% FBS and 1× penicillin-streptomycin. Both cell lines were maintained at 37 °C in a humidified incubator with 5% CO_2 and routinely tested for mycoplasma contamination. For tumor implantation, B16F10 or MC38 cells (5×10^5 cells per mouse, resuspended in 100 μL of buffer) were injected subcutaneously into the dorsal region of female C57BL/6 mice. Tumor length (L) and width (W) were measured using calipers, and tumor volume was calculated as $V = (L \times W^2)/2$.

In vivo intervention and combination therapy

Intraperitoneal injections were administered to mice 12 h after CLP induction as follows: anti-Gr1 antibody (10 mg/kg, Bio X Cell), Ly6G antibody (10 mg/kg, Bio X Cell), KU55933 (10 mg/kg, Cayman Chemical), NADPH (4 mg/kg, Sigma), or AS1842856 (15 mg/kg, MCE). Sham-operated and model groups received intraperitoneal injections of an equal volume of phosphate-buffered saline (PBS). Survival was monitored daily for 7 consecutive days across all groups. For the *in vivo* glucose-rescue experiment, CLP mice received a single intraperitoneal injection of D-glucose (1 g/kg) or an equivalent volume of normal saline at 24 h after surgery. Bone marrow, spleen, peripheral blood, lymph nodes, and peritoneal lavage fluid were collected 48 h after injection for flow-cytometric analysis of T-cell senescence-associated markers.

In the B16F10 tumor model, intraperitoneal injections of anti-Gr1 antibody (10 mg/kg, Bio X Cell), KU55933 (10 mg/kg, Cayman Chemical), or NADPH (4 mg/kg, Sigma) were administered on days 7, 11, and 15 after subcutaneous tumor implantation. Anti-PD-L1 antibody (2.5 mg/kg, Bio X Cell) was administered intraperitoneally on days 9, 13, and 17. Control mice received an equal volume of vehicle. Detailed information on reagents and antibodies is provided in Supplementary Table 2 and 3.

Bone marrow cell isolation and MDSCs induction

Bone marrow cells were flushed from the tibia and fibula of mice using sterile PBS. Red blood cells were lysed with red blood cell lysis buffer for 7 min at room temperature, followed by washing with PBS. Bone marrow cells were resuspended in RPMI 1640 supplemented with 10% FBS at a density of 2.5×10^5 cells/mL, supplemented with GM-CSF and IL-6 (final concentration, 40 ng/mL each; PeproTech), and cultured at 37 °C in a humidified incubator with 5% CO_2 for 4 days. Cells were then collected and purified using an MDSC negative isolation kit (StemCell Technologies). Detailed information on magnetic beads used for cell isolation is provided in the Supplementary Table 4.

Naïve T cell isolation and coculture

Mouse spleens were mechanically dissociated through a 70-μm cell strainer to generate single-cell suspensions. After erythrocyte lysis, splenocytes were washed with PBS. Naïve $CD4^+$ and naïve $CD8^+$ T cells were isolated using a negative isolation kit (StemCell Technologies) according to the manufacturers' instructions. Unless otherwise specified, all *in vitro*

experiments were performed on culture plates coated with anti-CD3 antibody (5 μg/mL; Invitrogen) and supplemented with anti-CD28 antibody (5 μg/mL; Invitrogen) and recombinant IL-2 (50 U/mL; PeproTech). Cells were cultured in RPMI 1640 medium (Gibco) supplemented with 10% heat-inactivated FBS (Gibco), 1% penicillin-streptomycin (Gibco), 2 mM L-glutamine (Gibco), and 50 μM 2-mercaptoethanol (Gibco).

Naïve $CD4^+$ or $CD8^+$ T cells (4×10^5 cells) were cocultured with MDSCs (1×10^5 cells) at a 4:1 (T cell:MDSC) ratio for 3 days. To maintain consistent total cell numbers and densities, control groups were supplemented with an equivalent number of T cells to match the total cell count in the coculture groups. To assess contact-dependent effects, MDSCs were fixed with 2% paraformaldehyde (Solarbio) for 20 min, washed three times with PBS, and subsequently used for coculture with naïve T cells. For preparation of MDSC-conditioned medium, induced MDSCs were washed three times with PBS to thoroughly remove residual cytokines and components of the original culture medium. The cells were then seeded at a density of 1×10^6 cells/mL in RPMI 1640 medium supplemented with 10% FBS and cultured for 24 h. The supernatant was then collected and centrifuged at 500 × g for 5 min to remove intact cells, followed by centrifugation at 2,000 × g for 10 min to remove cellular debris, and subsequently filtered through a 0.22-μm membrane. The clarified supernatant was used as MDSC-conditioned medium for subsequent experiments. To assess whether MDSC-induced T cell senescence is contact dependent, MDSCs and T cells were indirectly cocultured for 3 days using Transwell inserts with a 0.4-μm pore size (Corning). The upper chamber was pre-coated with anti-CD3 antibody (5 μg/mL, Invitrogen) before seeding T cells (4×10^5 cells per upper chamber), whereas the lower chamber was seeded with MDSCs (1×10^5 cells per lower chamber), and the culture medium was supplemented with anti-CD28 antibody (5 μg/mL, Invitrogen) and recombinant IL-2 (50 U/mL, Peprotech). The inhibitors were used in the experiments at concentrations determined to be non-toxic (Fig. S1A-D). For inhibitor pretreatment experiments, naïve T cells were pretreated with AS1842856 (5 μM) or Compound C (5 μM), whereas MDSCs were pretreated with phloretin (2 μM) or 2-DG (1 mM) for 24 h. Following pretreatment, the cells were washed and cocultured for 3 days, without further inhibitor supplementation during coculture.

T cell proliferation assay

$CD8^+$ T cells (1×10^6 cells/mL) were labeled with Violet Proliferation Dye 450 (1 μM; BD Biosciences) in PBS for 15 min in the dark, followed by two washes with RPMI 1640 medium containing 10% FBS. Labeled T cells were then cultured alone or cocultured with MDSCs for

72 h on plates pre-coated with anti-CD3 antibody (5 μg/mL; Invitrogen) and supplemented with soluble anti-CD28 antibody (5 μg/mL; Invitrogen) and recombinant IL-2 (50 U/mL; PeproTech).

T-cell functional assessment

For effector-function and exhaustion-marker analyses, naïve $CD8^+$ T cells were cultured alone or cocultured with MDSCs under anti-CD3/CD28 stimulation for 3 days, followed by flow-cytometric assessment of IFN-γ, perforin, granzyme B, PD-1, TIM-3, and TOX. For the anergy positive control, naïve $CD8^+$ T cells were stimulated with plate-bound anti-CD3 alone (5 μg/mL) for 48 h, rested for 24 h, and then rechallenged with anti-CD3/CD28 (5 μg/mL each) for 72 h in the presence or absence of IL-2 (50 U/mL). Proliferation was assessed by VPD450 dilution. For the AICD assay, an AICD-positive control was generated by activating $CD8^+$ T cells with plate-bound anti-CD3 and anti-CD28 antibodies (5 μg/mL each) plus IL-2 (100 U/mL) for 48 h, followed by 24 h of IL-2 expansion. Control, MDSC-treated, and AICD-positive-control T cells were then restimulated with plate-bound anti-CD3 (5 μg/mL) for 6 h in the absence of IL-2, and cell death was assessed by Annexin V and 7-AAD, Caspase-3/7 and 7-AAD staining. For coculture intervention experiments, MDSC-treated $CD8^+$ T cells were collected after 72 h of coculture, MDSCs were removed, and the T cells were subsequently treated with vehicle, anti-PD-1 blocking antibody (10 μg/mL), or D+Q (dasatinib, 10 nM; quercetin, 10 μM) for 24 h. SA-β-gal activity and proliferative capacity were subsequently assessed by flow cytometry.

Senescence-associated-β-galactosidase (SA-β-gal) assay

T cell senescence was assessed using a SA-β-gal assay kit (DOJINDO). Following coculture, cells were stained according to the manufacturer's protocol, and SA-β-gal fluorescence intensity was analyzed by flow cytometry. Detailed information on the SA-β-gal assay kit is provided in Supplementary Table 2.

ROS and Mitochondrial function assay

Intracellular ROS levels were detected using CellROX™ Green reagent (Invitrogen). Cells were treated at the indicated concentrations and incubation times and incubated at 37 °C in the dark. After washing, samples were analyzed by flow cytometry using a BD LSRFortessa.

Mitochondrial parameters were assessed using MitoSOX™, MitoTracker™ Green FM, and tetramethylrhodamine methyl ester (TMRM, Invitrogen) at the indicated concentrations and incubation times according to the manufacturers' instructions. Following washing steps,

samples were analyzed by flow cytometry or imaging-based analysis. Detailed information on these reagents is provided in Supplementary Table 2.

Flow cytometry

Cell surface staining was performed at room temperature in the dark for 30 min, with 7-AAD used to exclude dead cells. Intracellular protein staining was carried out using the BD Cytofix/Cytoperm™ kit and BD Perm/Wash™ buffer (BD Biosciences). Nuclear transcription factor staining was performed using the BD Pharmingen™ Transcription Factor Buffer Set (BD Biosciences). Phosphorylated proteins were detected following fixation with BD Phosflow™ Fix Buffer I and permeabilization with BD Phosflow™ Perm Buffer III (BD Biosciences), according to the manufacturers' instructions.

For intracellular cytokine staining, cells were stimulated with anti-CD3/CD28 antibodies (5 μg/mL; Invitrogen), and GolgiPlug™ protein transport inhibitor (BD Biosciences) was added during the final 6 h of incubation. Intracellular cytokines were subsequently detected by flow cytometry. Detailed information on antibodies used for flow cytometry is provided in Supplementary Table 2. Samples were acquired on a BD LSRFortessa flow cytometer and analyzed using FlowJo software (v10.8). The T cell gating strategy and fluorescence minus one (FMO) were shown in Fig. S1E.

Imaging flow cytometry and colocalization analysis

Samples underwent multicolor fluorescent staining and were acquired on ImageStream®X Mk II for analysis with IDEAS®. Valid events were filtered using quality focus and single-cell gating criteria. Spatial colocalization between signaling molecules and senescence markers was quantified using IDEAS's built-in colocalization/similarity metrics.

Blocking experiments

T cells were pretreated for 24 h with an anti-PD-1 blocking antibody (10 μg/mL; clone 29F.1A12), the Adenosine A2A receptor (A2AR) antagonist ZM241385 (100 μM), or an anti-IL-10R blocking antibody (10 μg/mL; clone 1B1.3a), followed by washing and coculture with MDSCs for 3 days. These agents were not maintained during coculture to minimize their direct effects on MDSCs and to assess the effects of T-cell pretreatment. The Arg1 inhibitor nor-NOHA (200 μM), the iNOS inhibitor L-N6-(1-iminoethyl)lysine (L-NIL; 10 μM), and a TGF-β-neutralizing antibody (10 μg/mL; clone 1D11) were added at the initiation of coculture and maintained throughout the 3-day culture period. Corresponding vehicle or isotype controls were

included in all experiments. Detailed information on these reagents is provided in Supplementary Table 3.

2-(N-(7-Nitrobenz-2-oxa-1,3-diazol-4-yl)Amino)-2-Deoxyglucose (2-NBDG) glucose uptake assay *in vitro* and *in vivo*

In vitro glucose uptake assays were performed by adding 2-NBDG (50 μM, Invitrogen) to the culture medium, followed by incubation at 37 °C in the dark for 30 min. Cells were then washed with PBS and analyzed by flow cytometry. For *in vivo* glucose uptake assays, CLP mice, B16F10- or MC38- bearing mice were intravenously injected via the tail vein with 100 μL of PBS containing 5 mM 2-NBDG. One hour after injection, mice were euthanized, and peripheral blood and tissues were harvested and processed into single-cell suspensions. 2-NBDG uptake in MDSCs and T cells was analyzed by flow cytometry in peripheral blood, spleen, bone marrow, and relevant lymph nodes or tumor tissues.

Seahorse extracellular flux analysis

Following coculture, T cells were seeded at 1×10^5 cells per well onto XF24 cell culture microplates (Agilent) pre-coated with Cell-Tak (22 μg/mL; Corning). Oxygen consumption rate (OCR) was measured using Seahorse XF RPMI medium (Agilent) supplemented with glutamine (2 mM, Gibco), glucose (10 mM, Agilent), and sodium pyruvate (1 mM, Agilent), with sequential injection of oligomycin (2 μM, Agilent), FCCP (1 μM, Agilent), and rotenone/antimycin A (0.5 μM, Agilent). Extracellular acidification rate (ECAR) was measured in XF Basal Medium supplemented with glutamine (2 mM, Gibco) only, followed by sequential addition of glucose (10 mM, Agilent), oligomycin (1 μM, Agilent), and 2-DG (50 mM, Agilent). All experiments were performed using an XF24 extracellular flux analyzer (Seahorse Bioscience). Detailed information on reagents used for Seahorse extracellular flux analysis is provided in Supplementary Tables 2-5.

Metabolite assays

Equal numbers of naïve T cells or MDSCs were cultured separately for 3 days. Culture supernatants were collected, and residual glucose levels were measured using a Glucose assay kit (Sigma) according to the manufacturer's instructions. Naïve T cells (4×10^5 cells) were cocultured with MDSCs (1×10^5 cells) for 3 days. As a control, naïve T cells cultured alone (5×10^5 cells) were used to match the total cell number in the coculture condition. After 3 days of culture, T cells were isolated from the coculture system using magnetic bead-based separation.

Subsequently, 3×10^5 sorted T cells from either the coculture group or the control group were collected for downstream experiments. Intracellular GSH/GSSG levels, $NADPH/NADP^+$ levels, 6-phosphogluconate dehydrogenase (6PGD) activity, and glucose-6-phosphate (G6P) content were measured using commercial assay kits (BioVision, Amplite, and Abcam) Standard curves were generated, and data were analyzed according to the manufacturers' instructions. Detailed information on these assay kits is provided in Supplementary Table 4.

qRT-PCR

After coculture, T cells were re-isolated using magnetic beads (StemCell Technologies). Total RNA was extracted using the RNeasy kit (Qiagen) and quantified using a NanoDrop spectrophotometer. Reverse transcription was performed using SuperScript™ IV (Invitrogen). qRT-PCR was conducted using a QuantStudio 3 system. β-Actin served as the internal control, and relative gene expression was calculated using the 2^−ΔΔCt method. Primer sequences used for qRT-PCR are listed in Supplementary Table 6.

ELISA

Blood samples were collected from CLP or sham-operated mice by retro-orbital bleeding. After clotting at room temperature, serum was obtained by centrifugation at 4 °C and stored at -20 °C until analysis. Serum levels of IL-6, IL-1β, TNF-α, and IFN-γ were measured using mouse ELISA kits (Invitrogen) according to the manufacturer's instructions. For T cell-conditioned supernatants, naïve $CD8^+$ T cells were cultured alone or with MDSCs in a Transwell system for 3 days, then washed and cultured in fresh medium for an additional 24 h before supernatant collection. IL-1β levels were measured by ELISA. Detailed information on ELISA kits is provided in Supplementary Table 4.

Western blot analysis

After coculture of naïve $CD8^+$ T cells with MDSCs for 3 days, $CD8^+$ T cells were isolated using magnetic beads (StemCell Technologies). Proteins were extracted using RIPA buffer (Beyotime) supplemented with protease and phosphatase inhibitors, separated by SDS-PAGE (Thermo), and transferred onto membranes. Membranes were incubated with primary antibodies overnight at 4 °C, followed by incubation with HRP-conjugated secondary antibodies at room temperature and detection by chemiluminescence. Detailed information on antibodies used for western blotting is provided in Supplementary Tables 2 and 8

Immunofluorescence assay

After coculture, cells were prepared as suspension cell smears and fixed. Immunofluorescence staining was performed using antibodies against CD8a and FOXO1 (eBioscience), followed by counterstaining with DAPI (Vector Laboratories). Images were acquired using a confocal microscope (Zeiss). For tissue multiplex immunofluorescence, sections were subjected to antigen retrieval in Tris-EDTA buffer (pH 8.0) for 15 min and blocked with serum or BSA. Sections were sequentially incubated with primary antibodies against CD8, CD11b, Gr1, and Foxp3, followed by the corresponding HRP-conjugated secondary antibodies and tyramide signal amplification (TSA) fluorophores. Primary antibodies were incubated at 4°C overnight, and antibody complexes were stripped between successive staining cycles to allow sequential detection of multiple markers. After completion of staining, nuclei were counterstained with DAPI, and fluorescence images were acquired using a digital slide scanner (Servicebio). The mean nearest-neighbor distances from $CD8^+$ T cells to $Gr1^+$ myeloid cells or $Foxp3^+$ Tregs were quantified in CLP spleen and B16F10 tumor tissues. Detailed information on antibodies used for immunofluorescence is provided in Supplementary Table 2.

Targeted metabolomics analysis

After coculture of naïve $CD8^+$ T cells with MDSCs for 3 days, $CD8^+$ T cells were isolated using magnetic beads (StemCell Technologies). Metabolites were extracted using a methanol/acetonitrile/water mixture (2:2:1, v/v/v), spiked with isotopically labeled internal standards, vacuum-dried, and reconstituted prior to analysis. Metabolite detection was performed using UPLC-MS/MS (QTRAP 5500) in multiple reaction monitoring (MRM) mode. Peak areas were extracted and relatively quantified using MultiQuant software. Protein content was measured for data normalization, and quality control (QC) samples were interspersed throughout each batch to monitor analytical stability. Differences in metabolite abundance between the two groups were assessed using unpaired two-tailed Student's t-tests. P values were adjusted for multiple testing across the analyzed metabolites using the Benjamini–Hochberg procedure, with an FDR threshold of 0.05.

Bulk RNA sequencing (RNA-seq) and assay for transposase-accessible chromatin with high-throughput sequencing (ATAC-seq) analysis

After coculture of naïve $CD8^+$ T cells with MDSCs for 3 days, $CD8^+$ T cells were isolated using magnetic beads (StemCell Technologies). For bulk RNA-seq, total RNA was extracted using TRIzol reagent, followed by library preparation and high-throughput sequencing. Sequencing

reads were aligned to the reference genome using HISAT2, and gene expression levels were quantified using RSEM. Differential gene expression analysis was performed using DESeq2 with a cutoff of $|\log_2 \text{fold change}| \geq 0.5$ and adjusted P value ≤ 0.05. Gene Set Enrichment Analysis (GSEA) was conducted using the clusterProfiler package, with Benjamini–Hochberg-adjusted $P < 0.05$ considered significant.

For ATAC-seq, nuclei were extracted from the isolated cells (approximately 50,000 nuclei per sample), followed by Tn5 transposase-mediated tagmentation at 37 °C for 30 min for library preparation and sequencing. Raw FASTQ files were subjected to quality control, and sequencing reads were aligned to the reference genome using BWA. Peaks were identified using MACS2 with a q-value threshold of < 0.05. Motif analysis was performed using HOMER, and differential peak analysis, annotation, and enrichment analysis were conducted using bedtools.

Public cohort and single-cell RNA sequencing (scRNA-seq) datasets analysis

Public scRNA-seq datasets GSE152275, GSE139125, and GSE249975 were analyzed in R 4.2.3 using Seurat v5.1.0 and harmony v1.2.0. Seurat objects were initially generated with a minimum of 3 cells per gene and 300 detected features per cell. Cells were retained if they contained >300 and <8000 detected genes, >1000 total RNA counts, nCount_RNA below the 97th percentile of the corresponding sample, <10% mitochondrial transcripts, and <3% hemoglobin-related transcripts. After merging, expression matrices were normalized using the LogNormalize method, 3000 highly variable genes were selected using the vst method, and the data were scaled before principal-component analysis. Batch effects across samples were corrected using Harmony with sample identity as the grouping variable. The main cell atlas was constructed using Harmony dimensions 1 – 10 with a clustering resolution of 0.5, followed by UMAP visualization. Marker genes were identified using the Wilcoxon rank-sum test with a log2 fold-change threshold of 0.25, and P values were adjusted for multiple testing using the Bonferroni method, with Bonferroni-adjusted $P < 0.05$ considered statistically significant. For GSEA/enrichment analyses based on scRNA-seq data, multiple testing was controlled using the Benjamini–Hochberg procedure. Cell–cell communication was analyzed using CellChat v2.1.2, and single-cell metabolic activity was evaluated using scMetabolism v0.2.1. For bulk/public-cohort signature scoring, GSVA/ssGSEA was performed using GSVA v1.52.3. Standard pathway gene sets were obtained from the Molecular Signatures Database (MSigDB). Specifically, REACTOME_CELLULAR_SENESCENCE was used for cellular senescence, GOBP_DNA_DAMAGE_RESPONSE for DNA-damage responses, HALLMARK_GLYCOLYSIS for glycolysis,

REACTOME_PENTOSE_PHOSPHATE_PATHWAY for the pentose phosphate pathway, HALLMARK_REACTIVE_OXYGEN_SPECIES_PATHWAY for reactive oxygen species-related signaling, and HALLMARK_FATTY_ACID_METABOLISM for fatty-acid metabolism. Literature-defined T cell senescence, T_{TAD}, and MDSC-associated signatures were obtained from their respective original publications [13, 35].

Statistical analysis

Statistical analyses were performed using GraphPad Prism 9.0 and R 4.2.3. Unless otherwise specified, n represents the number of independent biological replicates. For *in vivo* experiments, each mouse was treated as one biological replicate; for human studies, each participant was treated as one biological replicate; and for *in vitro* experiments, n represents independent biological experiments. Technical replicates, when performed, were averaged within each biological replicate before statistical analysis and were not treated as independent observations. Comparisons between two independent groups were performed using an unpaired two-tailed Student's t-test. Paired two-tailed Student's t-test was used for paired measurements obtained from the same biological replicate. Comparisons among three or more independent groups were analyzed using one-way ANOVA followed by Tukey's test for pairwise comparisons or Dunnett's test for comparisons of multiple treatment groups with a single control. Two-factor experiments involving independent observations were analyzed using two-way ANOVA followed by Šídák's multiple-comparisons test. For measurements obtained from multiple tissues of the same mouse, tissue was treated as a within-subject repeated factor and experimental group as a between-subject factor using two-way repeated-measures ANOVA, followed by Šídák's multiple-comparisons test for comparisons between experimental groups within each tissue; a mixed-effects model with mouse identity as the random effect was used when repeated measurements were incomplete. Longitudinal tumor-growth data were analyzed using two-way repeated-measures ANOVA, and Kaplan–Meier survival curves using the log-rank (Mantel–Cox) test. Pearson's correlation was used for independent biological observations. Benjamini–Hochberg FDR correction was applied within the relevant hypothesis families to differential-expression analysis of bulk RNA-seq data using DESeq2, GSEA enrichment analyses based on bulk RNA-seq, scRNA-seq, and ATAC-seq data, targeted metabolomics comparisons, and multiple correlation analyses across public cohorts. For scRNA-seq marker-gene analysis, P values were adjusted for multiple testing using the Bonferroni method. Statistical significance was defined as $P < 0.05$ for conventional statistical comparisons, BH-adjusted $P < 0.05$ for analyses using Benjamini–Hochberg correction, or Bonferroni-adjusted P

475 < 0.05 for scRNA-seq marker-gene analysis. Bulk RNA-seq (n = 2) was used as an exploratory
476 screening approach, with key findings subsequently validated by qRT-PCR, flow cytometry,
477 and functional assays.
478

Results

MDSCs promote T cell senescence

To determine whether MDSCs contribute to T cell senescence, we first evaluated their expansion and correlation with senescent T cells in CLP models and tumor-bearing mouse models. Following CLP induction, MDSCs progressively accumulated during disease progression from day 1 to day 7, accompanied by increased SA-β-gal activity in $CD8^+$ and $CD4^+$ T cells across multiple tissues. MDSC frequency was positively correlated with SA-β-gal levels in both $CD8^+$ and $CD4^+$ T cells across tissues (Fig. S2A-G). Similarly, both MDSC expansion and increased T cell SA-β-gal levels were observed in B16F10- and MC38-bearing mice (Fig. S3A-F). To further evaluate senescence score across different cell populations, we analyzed public scRNA-seq datasets. T cell populations in both the CLP and tumor datasets exhibited increased senescence signature score (Fig. S3G). To characterize senescent T cell subsets, we adopted the gene signature defined by Chen et al. for tumor-infiltrating, age-associated dysfunctional T cells (T_{TAD}), a recently identified population linked to extracellular senescence signals [13]. Consistent with this characterization, analysis of public scRNA-seq datasets revealed an increased abundance of T_{TAD} cells within T cells in CLP or tumor-bearing mice relative to controls (Fig. S3H). Furthermore, positive correlations of both the T_{TAD} gene signature and an independent T cell senescence signature with the MDSC-associated gene signature were observed across sepsis and multiple tumor datasets from GEO and TCGA (Fig. S4A, B) [35]. In line with this, patients with sepsis and hepatocellular carcinoma exhibited markedly higher levels of SA-β-gal, p16, and p21 in peripheral-blood $CD8^+$ and $CD4^+$ T cells than healthy controls. Moreover, we observed an increase in circulating MDSCs, which positively correlated with multiple senescence-associated markers in T cells within the HC and sepsis participants (Fig. S4C-F).

Given the role of Tregs in promoting T cell senescence [22, 36], we further compared MDSC-T cell and Treg-T cell interactions by analyzing public scRNA-seq data from CLP mice. It was revealed that MDSCs engage in more extensive intercellular communication than Tregs within the infection microenvironment (Fig. 1A, B). Further analysis positioned MDSCs as primary signaling senders, with $CD8^+$ T cells identified as major receivers (Fig. 1C). Multiplex immunofluorescence analysis of spleen tissues from CLP mice and tumor tissues from B16F10-bearing mice showed marked spatial proximity between $CD8^+$ T cells and $Gr1^+$ myeloid cells . Quantitative analysis showed that the nearest-neighbor distance between $CD8^+$ T cells and $Gr1^+$ myeloid cells was significantly shorter than that between $CD8^+$ T cells and $Foxp3^+$ Tregs (Fig. S5A, B). Collectively, these observations suggested that MDSCs might facilitate T cell

senescence through direct cellular communication. To validate this hypothesis, we conducted an *in vitro* coculture system of MDSCs and naïve T cells, according to the co-culture system of Tregs and naïve T cells described by Peng et al. (Fig. S6A) [22]. MDSCs were induced from bone marrow progenitor cells of 6- to 8-week-old mice using GM-CSF and IL-6 for 4 days, achieving over 90% purity and significant suppression of $CD8^+$ T cell proliferation (Fig. S6B). After coculture with MDSCs for 3 days, $CD8^+$ or $CD4^+$ T cells exhibited pronounced upregulation of senescence markers, including elevated SA-β-gal activity and increased expression of the cell-cycle regulatory molecules p53, p21, and p16 (Fig. 1D-G). Additionally, our bulk RNA-seq analysis showed significantly upregulated expression of genes associated with the SASP in cocultured T cells, which was validated by quantitative real-time PCR (qRT-PCR) in both $CD8^+$ and $CD4^+$ T cells (Fig. 1H-J). Consistently, at the protein level, we detected increased intracellular expression of key SASP factors, including pro-IL-1β, IL-6, and TNF-α (Fig. 1K, L). ELISA showed increased IL-1β levels in conditioned supernatants from MDSC-exposed $CD8^+$ T cells (Fig. S6C). To better recapitulate the inflammatory and tumor microenvironments, we evaluated MDSC-induced T cell senescence in the presence of LPS or B16F10 cell-conditioned medium. These conditions alone increased baseline SA-β-gal, p21, and p16 levels in $CD8^+$ T cells, while the addition of MDSCs further enhanced these senescence-associated changes (Fig. S6D, E). In summary, these findings identify MDSCs as a potent driver of T cell senescence.

Considering that T cell senescence, exhaustion, and anergy all manifest as varying degrees of functional impairment, we systematically analyzed the gene signatures of exhaustion and anergy states in MDSC-induced senescent T cells [37-39]. These cocultured $CD8^+$ T cells exhibited changes in exhaustion- and anergy-associated genes without a consistent transcriptional pattern (Fig. S7A, B). In agreement with this, ATAC-seq analysis demonstrated marked remodeling of chromatin accessibility of senescence-related genes, whereas exhaustion- and anergy-associated genes showed less consistent changes (Fig. S7C-F). Flow cytometry analysis revealed that while MDSC-cocultured $CD8^+$ T cells exhibited upregulation of certain surface markers (PD-1 and TIM-3), the expression of TOX, a key transcription factor associated with terminal exhaustion, remained unchanged (Fig. S8A). Recognizing that such alterations serve primarily as exploratory marker changes rather than a formal diagnostic classification, we utilized specific functional assays to further discriminate these states. Functionally, MDSC-treated $CD8^+$ T cells retained substantial IFN-γ production capacity and comparable perforin expression, although granzyme B expression was reduced, which is less consistent with a severely dysfunctional terminally exhausted phenotype (Fig. S8B).

Additionally, their proliferative defect was refractory to exogenous IL-2 rescue, rendering classical anergy unlikely (Fig. S8C). Furthermore, to functionally distinguish senescence from activation-induced cell death (AICD), we assessed apoptosis following TCR restimulation. MDSC-treated $CD8^+$ T cells exhibited significantly reduced apoptosis and higher viability compared with T cells cultured alone, whereas AICD-positive controls showed markedly increased apoptosis (Fig. S8D,E). Moreover, senolytic treatment with dasatinib and quercetin (D+Q) decreased SA-β-gal levels and improved proliferative capacity, whereas PD-1 blockade only partially restored proliferation without reducing SA-β-gal activity (Fig. S8F). Taken together, these specific molecular and functional findings indicate that MDSCs induce a predominant phenotype functionally consistent with T cell senescence.

ATM-dependent DDR is required for MDSC-induced T cell senescence

Considering that DNA damage induction represents a key molecular process in senescent cells [40, 41], we analyzed public scRNA-seq data and found an enrichment of gene sets associated with T cell senescence and DNA damage in tumor or infectious microenvironments derived from CLP or breast cancer mouse models that are abundant in MDSCs (Fig. 2A, B; Fig. S9). To determine whether DNA damage acts as a major trigger for senescence in T cells treated with MDSCs, we performed integrative enrichment analyses using both RNA-seq and ATAC-seq datasets. GSEA of RNA-seq data demonstrated robust activation of DNA damage-associated gene programs in MDSC-treated senescent $CD8^+$ T cells (Fig. 2C). Consistent with the transcriptomic profile, ATAC-seq analysis revealed increased chromatin accessibility at DNA damage-related signatures in cocultured $CD8^+$ T cells (Fig. 2D). We then evaluated DNA damage levels by assessing phosphorylated ATM, H2AX, and CHK2 in cocultured T cells via flow cytometry. The results showed markedly increased expression of these DNA damage markers in both $CD8^+$ and $CD4^+$ T cells following 3 days of MDSCs coculture compared with independently cultured controls, indicating that MDSCs induce a substantial DDR in T cells (Fig. 2E, F).

To establish a causal role of ATM-associated DNA damage in MDSC-induced T cell senescence, we employed a loss-of-function approach using the ATM-specific pharmacological inhibitor KU55933. To prevent potential interference of KU55933 with MDSCs, naïve $CD8^+$ and $CD4^+$ T cells were pretreated with KU55933 for 24 h, after which the inhibitor was washed out before co-culture with MDSCs. This pretreatment significantly attenuated SA-β-gal activity in responder T cells induced by MDSCs, indicating that activation of the ATM-dependent DDR is required for MDSC-mediated T cell senescence (Fig. 2G, H). To further explore the functional

relationship between DNA damage signaling and cell-cycle arrest during T cell senescence, we conducted co-localization analysis by using imaging flow cytometry. DNA damage markers including p-ATM, p-H2AX, and p-CHK2 exhibited strong intracellular co-localization with the cell-cycle regulators p16 and p21 in MDSC-induced senescent $CD8^+$ T cells, suggesting coordinated activation of DDR and senescence-associated cell-cycle arrest programs (Fig. 2I). Together, these results demonstrate that MDSCs induce T cell senescence, which correlates with cell-cycle arrest, through ATM-dependent DNA damage mechanisms.

MDSCs trigger T cell senescence through metabolic reprogramming induced by competitive glucose deprivation

To elucidate the specific mechanisms driving MDSC-mediated T cell senescence, we systematically investigated classical immunosuppressive modalities to exclude contact-dependent and conventional soluble mediators. We observed that paraformaldehyde-fixed MDSCs failed to induce T cell senescence, whereas transwell and conditioned medium cultures preserved the senescent phenotype, suggesting that the induction of senescence necessitates live MDSCs but operates independently of direct cell-to-cell contact (Fig. 3A). Despite the elevated surface abundance of PD-L1, CD39, and CD73 on MDSCs (Fig. S10A-C), neither PD-1 blockade nor antagonism of adenosine A2A receptors alleviated the senescent phenotype (Fig. S10D-K). Similarly, Arg1 blockade, NOS2 blockade, TGF-β neutralization, and IL-10 receptor blockade failed to rescue T cells from senescence, indicating that this process is driven by a mechanism distinct from established receptor-ligand interactions or immunoregulatory factors (Fig. S11A-H, Fig. S12A-H).

We therefore hypothesized that the rapid consumption of extracellular nutrients by MDSCs might promote T cell senescence through metabolic starvation. MDSCs exhibited significantly elevated expression of the rate-limiting glucose transporter glucose transporter 1 (GLUT1) and the glycolytic enzyme hexokinase 2 (HK2) compared with multiple T cell subsets in the peripheral blood of septic mice (Fig. 3B). Given that induced MDSCs comprised approximately 80% polymorphonuclear MDSCs (PMN-MDSCs) and 20% monocytic MDSCs (M-MDSCs), we separately compared GLUT1 and HK2 expression in each MDSC subset with that in T cells (Fig. S13A). Both MDSC subsets showed higher GLUT1 and HK2 expression than $CD4^+$ and $CD8^+$ T cells (Fig. S13B, C). This molecular signature translated into a superior functional capacity for glucose uptake, as MDSCs rapidly depleted glucose from the culture supernatant and exhibited significantly higher levels of the fluorescent glucose analog 2-NBDG than $CD8^+$ and $CD4^+$ T cells *in vitro* (Fig. 3C, D). We further confirmed this metabolic dominance *in vivo*,

where MDSCs from multiple tissues, particularly the peritoneal cavity of CLP-induced septic mice and the tumor microenvironment of both B16F10- and MC38-bearing mice, displayed markedly enhanced glucose uptake capacity compared to $CD8^+$ or $CD4^+$ T cells (Fig. 3E, F; Fig. S13D). The scMetabolism analysis and single-gene analysis in public scRNA-seq datasets confirmed these findings, revealing that MDSCs exhibited higher glucose metabolism scores and higher expression of glucose metabolism genes than Tregs in both sepsis and tumor microenvironments, with levels even comparable to malignant cells (Fig. 3G; Fig. S13E). Crucially, depleting $Gr1^+$ myeloid cells via anti-Gr1 administration in septic mice restored the glucose metabolic capacity of $CD8^+$ and $CD4^+$ T cells across multiple tissues (Fig. 3H, I; Fig. S14A-H).

To determine whether this competitive glucose deprivation drives the metabolic imbalance associated with senescence, we profiled the transcriptional landscape of glucose metabolism of cocultured $CD8^+$ T cells across multiple time points (0, 3, and 5 Days). RNA-seq analysis revealed a metabolic remodeling in T cells that peaked by day 3, characterized by the global suppression of genes encoding rate-limiting enzymes in glycolysis and the PPP (Fig. 4A; Fig. S15A). These transcriptomic observations were validated by qRT-PCR analysis of key metabolic enzymes (Fig. 4B-E). Flow cytometry and absorbance assay confirmed the downregulation of GLUT1 and HK2 (Fig. 4F, G), as well as critical PPP rate-limiting enzymes such as glucose-6-phosphate dehydrogenase (G6PD) and 6PGD, concomitant with a reduction in PPP substrate G6P levels (Fig. 4H, I). A comprehensive targeted metabolomics analysis further displayed this metabolic reprogramming, demonstrating a widespread depletion of key metabolites associated with glucose energy metabolism in MDSC-exposed $CD8^+$ T cells (Fig. 4J; Fig. S15B). This transcriptional and metabolite-level suppression resulted in a functional bioenergetic crisis, evidenced by diminished ECAR and OCR, along with a collapse in mitochondrial spare respiratory capacity and reduced ATP synthase F1 subunit alpha (ATP5A) expression (Fig. 4K-N).

To establish a causal link between glucose competition and MDSC-induced T cell senescence, we modulated the metabolic availability within the coculture system. Pharmacological inhibition of MDSCs glucose transport with phloretin or glycolysis with 2-deoxyglucose (2-DG) significantly attenuated their senescence-inducing potency, indicating the role of glucose metabolic activity of MDSCs (Fig. 4O, P). Notably, the exogenous supplementation of glucose into coculture was sufficient to prevent the onset of cellular senescence and simultaneously reduced the DDR in T cells, as evidenced by decreased phosphorylation of ATM, H2AX, and CHK2 (Fig. S15C, D). Together, our *in vitro* mechanistic findings provide evidence that

MDSCs drive T cell senescence and associated DNA damage through glucose competition and the subsequent metabolic reprogramming.

MDSC-induced metabolic stress drives T cell senescence via the AMPK-Foxo1 signaling axis

In order to elucidate the molecular mechanisms underlying MDSC-induced T cell senescence, we conducted Kyoto Encyclopedia of Genes and Genomes (KEGG) enrichment analysis of signaling pathways in $CD8^+$ T cells cocultured with MDSCs for 3 days. The results revealed significant alterations in several immune-related pathways, notably the TNF, cAMP, MAPK, and AMPK signaling cascades (Fig. 5A), all of which have been implicated in driving T cell senescence [22-24, 42]. In particular, the AMPK pathway is a strong candidate given its role as a central nutrient and energy sensor activated by metabolic stress [43-46]. Consistent with this, GSEA further demonstrated a robust upregulation of AMPK pathway-related genes, including Foxo1 (Fig. 5B). Subsequent screening for transcription factor significantly perturbed during MDSC-induced senescence also identified Foxo1 as a key regulator (Fig. 5C; Fig. S16A). It is known that Foxo1 activation can upregulate p16 and p21 and induce cell-cycle arrest [47-55]. These converging lines of evidence collectively prompted us to investigate into the role of AMPK-Foxo1 axis in MDSC-driven T cell senescence.

Foxo1 activity is finely tuned by site-specific phosphorylation, which dictates its subcellular localization. Specifically, phosphorylation of the conserved Ser256 residue by the PI3K/AKT signaling pathway facilitates its nuclear export, leading to inactivation. Conversely, under conditions of metabolic stress, AMPK activation is associated with increased Foxo1 phosphorylation at Ser249 and its nuclear translocation, potentially contributing to the activation of Foxo1-dependent transcriptional programs [56, 57]. In light of this regulatory switch, we investigated the changes in Foxo1 phosphorylation patterns to define the potential mechanistic role of AMPK-Foxo1 pathway during MDSC-induced immunosenescence. Flow cytometry analysis revealed a time-dependent elevation in the total expression of Foxo1 as the coculture period with MDSCs increased, characterized by a marked increase in phosphorylation at Ser249 rather than Ser256 (Fig. 5D, E). Consistently, the phosphorylation level of AMPK was notably upregulated, while the AKT signaling pathway remained unchanged (Fig. 5F, G; Fig. S16B). The upregulation of AMPK phosphorylation in T cells was also observed across tissues in the CLP model (Fig. S16C, D), supporting the presence of widespread energetic stress in T cells during CLP. These results were further confirmed by western blot analysis. Of note, pFoxo1(Ser249) was upregulated in the nucleus of cocultured $CD8^+$ T cells, whereas

pFoxo1(Ser256) was primarily confined to the cytoplasm (Fig. 5H, I). Both immunofluorescence and imaging flow cytometry validated that phosphorylation of Foxo1 at Ser249 rather than Ser256 facilitated its nuclear accumulation in MDSC-induced senescent $CD8^+$ T cells (Fig. 5J-L). ATAC-seq analysis demonstrated a significant increase in the chromatin accessibility of *Foxo1* and its target gene *Cdkn2a* (Fig. 5M). Imaging flow cytometry revealed that pAMPK and pFoxo1(Ser249) respectively exhibited high co-localization with DNA damage markers and cell-cycle regulatory molecules in MDSC-induced senescent $CD8^+$ T cells (Fig. 5N). More importantly, pretreatment of naïve T cells with inhibitors targeting AMPK-Foxo1 axis significantly attenuated the senescent phenotype induced by MDSCs, emphasizing the regulatory role of AMPK-Foxo1 pathway in driving T cell senescence (Fig. 5O, P; Fig. S17A, B).

To assess whether glucose restriction alone is sufficient to directly activate AMPK and drive senescence, we cultured naïve T cells in media containing a range of decreasing glucose concentrations (0-10 mM). Exposure to low-glucose conditions induced the upregulation of AMPK phosphorylation and senescence markers in a dose-dependent manner (Fig. S17C, D). Similarly, treating naïve T cells with 2-DG for 5 days significantly enhanced AMPK activity and expression of senescence markers (Fig. S17E, F). Taken together, these data indicate that MDSC-mediated glucose deprivation triggers an AMPK-Foxo1 signaling cascade that drives T cell senescence by enforcing cell-cycle arrest.

MDSC-mediated suppression of the PPP activity compromises T cell redox homeostasis and drives T cell senescence

Given that the PPP constitutes the principal cellular source of NADPH required for antioxidant defense [58], we hypothesized that the MDSC-imposed metabolic restriction precipitates T cell senescence by disrupting redox homeostasis. To investigate the hypothesis, we quantified the intracellular landscape of $NADPH/NADP^+$ and GSH/GSSG redox couples. Our analysis revealed a significant impairment of antioxidant capacity in T cells exposed to MDSCs, characterized by a depletion of the reduced coenzyme NADPH and a consequent inversion of the NADPH to $NADP^+$ ratio (Fig. 6A). This defect in upstream reducing equivalents was functionally transmitted to the downstream glutathione system, as evidenced by the scarcity of reduced glutathione and a concomitant accumulation of oxidized glutathione GSSG (Fig. 6B). Supporting these biochemical imbalances, GSEA indicated transcriptional downregulation of genes governing reactive oxygen species (ROS) clearance systems in T cells following coculture (Fig. 6C). RNA-seq heatmaps revealed alterations in glutamine and lipid metabolism (Fig. S18A,B), with

representative changes confirmed by RT-qPCR (Fig. S18C,D). Consistently, flow cytometry analysis exhibited a pronounced accumulation of intracellular ROS in cocultured T cells, confirming their heightened susceptibility to oxidative insults (Fig. 6D). This systemic failure in ROS scavenging manifested as severe mitochondrial dysfunction, characterized by an aberrant accumulation of mitochondrial superoxide, increased mitochondrial mass, and compromised membrane potential (Fig. 6E-G).

To establish a causal link between PPP impairment and the senescent phenotype, we performed metabolic rescue experiments by supplementing cocultures with exogenous reducing agents, including NADPH, glutamine, and GSH. Consistent with our hypothesis, these interventions effectively neutralized the intracellular ROS burden and markedly attenuated SA-β-gal activity alongside DNA damage signaling cascades, as evidenced by reduced phosphorylation of ATM, CHK2, and H2AX (Fig. 6H-J; Fig. S19A-C). Further granular analysis via imaging flow cytometry revealed a striking mutual exclusivity between the expression of the rate-limiting PPP enzyme G6PD and nuclear markers of senescence or DNA damage. Conversely, these damage markers exhibited robust intracellular co-localization with ROS (Fig. 6K). Notably, MDSC-exposed $CD8^+$ T cells exhibited a near-complete depletion of G6PD protein, which correlated tightly with the induction of p21 and p-ATM (Fig. 6K). Collectively, these data identify the impairment of PPP-mediated antioxidant defenses as a key driver of MDSC-induced T cell senescence. Remarkably, spatial similarity analysis further delineated the intrinsic connection between the dual metabolic axes revealed in this study. We observed significant nuclear co-localization between key components of the PPP-redox-DDR axis (e.g., ROS/p-ATM/p-H2AX/p-CHK2) and the AMPK-Foxo1 axis (e.g., p-AMPK/p-Foxo1/p16/p21/p53) within senescent populations (Fig. S20). This high degree of spatial convergence underscores that redox-driven DNA damage and AMPK-mediated bioenergetic stress may converge and integrate at the subcellular level, collectively enforcing and stabilizing the T cell senescence phenotype.

Systemic $Gr1^+$ or $Ly6G^+$ myeloid cells depletion and pharmacological interventions alleviate T cell senescence and protect against lethality and multiple organ dysfunction in septic mice

To evaluate the *in vivo* therapeutic potential of modulating these metabolic and signaling pathways, we initiated systemic interventions in septic mice 12 hours after CLP (Fig. 7A). Strikingly, depletion of $Gr1^+$ or $Ly6G^+$ myeloid cells (anti-Gr1 or anti-Ly6G Abs, depletion efficiency was shown in Fig. S21A, B), NADPH supplementation, or pharmacological

blockade of ATM signaling conferred a significant survival benefit, markedly extending the overall survival compared to the vehicle-treated septic group (Fig. 7B). Flow cytometric analysis of the anti-Gr1-/anti-Ly6G, NADPH-, KU55933-, and AS1842856-treated groups revealed that these interventions *in vivo* successfully reduced SA-β-gal activity in T cells from spleen, lymph nodes, bone marrow, and peripheral blood (Fig. 7C). In CLP-derived T cells, KU55933 or AS1842856 reduced p-ATM and SA-β-gal levels and partially restored activation and proliferation, whereas neither inhibitor had a detectable effect on sham-derived T cells. Importantly, these improvements were markedly attenuated after D+Q pretreatment (Fig. S22). These data reflect a differential pathway dependency under pathological stress. Furthermore, consistent with these interventions, systemic glucose supplementation in CLP mice also attenuated SA-β-gal activity in T cells across multiple tissues (Fig. S23). These findings suggest a pharmacologic association between the alleviation of immunosenescence and improved outcomes in CLP mice.

We next investigated whether this immunological restoration translated into protection against multiple organ dysfunction which is the primary driver of sepsis-associated mortality. Focusing on the lung as a critical target organ, we observed that untreated septic mice exhibited hallmark features of acute lung injury including alveolar wall thickening, vascular congestion, and extensive neutrophilic infiltration, when sham-operated mice maintained intact alveolar architecture. In contrast, treatment with anti-Gr1, NADPH, KU55933, or AS1842856 preserved alveolar integrity and substantially reduced the accumulation of inflammatory cells (Fig. 7D). Consistent with these histopathological improvements, quantification of lung wet-to-dry weight ratios confirmed that interventions effectively ameliorated pulmonary edema (Fig. 7E). Furthermore, ELISA profiling demonstrated that the reduction in T cell senescence was accompanied by a profound suppression of the cytokine storm, as evidenced by decreased serum levels of IL-1β, IL-6, TNF-α, and IFN-γ (Fig. 7F-I). Collectively, these data suggest that modulating metabolic and signaling pathways implicated in MDSC-induced T-cell senescence dampens the pathological immune responses associated with sepsis, attenuates organ injury, and improves survival in CLP mice.

Depletion of Gr1$^+$ myeloid cells and systemic pharmacological interventions targeting ROS-DNA damage pathways alleviate T cell senescence and potentiate the efficacy of PD-L1 blockade in the B16F10 melanoma model

Since preventing T cell senescence is a critical factor in maintaining antitumor immune function [23, 24], we investigated whether these systemic *in vivo* interventions could reactivate anti-

tumor immunity in B16F10 melanoma mouse model. To evaluate strategies that inhibit this senescence-inducing cascade at distinct regulatory nodes, we designed intervention regimens involving the depletion of $Gr1^+$ myeloid cells with anti-Gr1 antibody (Fig. S21C), the scavenging of excess ROS via exogenous NADPH supplementation, and the inhibition of DNA damage using KU55933. Following the subcutaneous implantation of 5×10^5 B16F10 tumor cells into C57BL/6 mice, we initiated these targeted monotherapies on days 7, 11, and 15 post-challenge as outlined in Fig. 8A. Longitudinal monitoring of tumor progression revealed that these systemic *in vivo* interventions significantly restrained tumor growth compared to untreated controls (Fig. 8B). To elucidate the cellular mechanisms underlying this tumor control, we analyzed tumor-infiltrating lymphocytes at day 24. All systemic intervention groups exhibited significantly increased tumor-infiltrating $CD8^+$ T cells with reduced senescence, along with markedly elevated expression of cytotoxic effector molecules granzyme B and perforin (Fig. 8C). Furthermore, these interventions reduced $CD8^+$ T cell senescence in tumor-draining lymph nodes, peripheral blood, spleen, and bone marrow of B16F10-bearing mice while enhancing granzyme B and perforin expression (Fig. 8D, Fig. S24A, B). These findings indicate that modulating these associated pathways produces significant antitumor effects.

To address the limited clinical response rates and acquired resistance associated with immune checkpoint blockade (ICB) therapy, we investigated whether modulating pathways associated with T-cell senescence could enhance the antitumor efficacy of PD-L1 blockade in the B16F10 melanoma model. We incorporated anti-PD-L1 antibody treatment into the existing regimen on days 9, 13, and 17 (Fig. 8E). This combination strategy produced enhanced antitumor efficacy, demonstrating substantially stronger tumor growth inhibition compared to ICB monotherapy (Fig. 8F). Analysis of tumor-infiltrating lymphocytes at day 24 revealed that compared to anti-PD-L1 monotherapy, the combination strategy significantly enhanced the enrichment of $CD8^+$ T cells within the tumor microenvironment (Fig. 8G) and more markedly alleviated T cell senescence phenotypes (Fig. 8H). Functionally, combination therapy significantly increased granzyme B and perforin expression in $CD8^+$ T cells (FIG. 8I, J). Consistently, similar outcomes were observed in various immune tissues of tumor-bearing mice treated with the combination approach (Fig. S24C-E). In summary, these data indicate that depletion of $Gr1^+$ myeloid cells and systemic pharmacological interventions targeting ROS-DNA damage pathways not only alleviate T cell senescence but also enhance the antitumor efficacy of PD-L1 blockade, supporting further evaluation of this combination strategy in tumor immunotherapy in the B16F10 melanoma model.

Discussion

MDSCs are established as principal immunoregulatory components within tumor and infectious microenvironments, where they potently suppress T cell proliferation and effector function through diverse mechanisms, thereby facilitating immune escape [59-64]. However, their specific role and mechanistic contribution to T cell senescence have remained largely unexplored. Here, through integrated multi-omics and functional validation, our findings support a role for MDSC-associated glucose competition in promoting T cell senescence. This process is not merely a byproduct of nutrient scarcity but a specialized mechanism of active metabolic remodeling that triggers a dual crisis: an AMPK/Foxo1-mediated energy stress and a PPP/NADPH-driven oxidative stress. Our findings characterize MDSCs as a critical metabolic checkpoint, thereby providing a conceptual foundation for therapeutic strategies targeting the metabolism-senescence axis.

Perhaps the most striking finding of our study is the identification of MDSCs as an upstream cellular driver of T cell senescence. Previous work by Liu et al. demonstrated that T cell senescence within the tumor microenvironment (TME) is primarily driven by metabolic competition jointly mediated by tumor cells and Tregs. Tumor cells are known to promote senescence through glucose competition or reprogramming T cell lipid metabolism, which was mediated via the secretion of PD-L1-bearing exosomes or ILT4-mediated MAPK/ERK pathway activation [22, 25, 26]. Similarly, Tregs trigger ATM/STAT-dependent DNA damage and cell-cycle arrest in T cells by high-affinity competition for IL-2 and glucose, or via phospholipase A2-IVA-dependent lipid remodeling [22, 36]. However, the fundamental contribution and precise mechanism of MDSCs in this pathological process has remained largely unexplored despite their ubiquity in the TME and infectious niches. Building upon the broader concept of metabolic competition, our study delineates the intracellular cascade triggered by MDSC-driven glucose deprivation. We demonstrate that the resulting bioenergetic and oxidative crises engage the AMPK/Foxo1 and PPP/NADPH axes to enforce a senescence program. This finding provides a novel mechanistic perspective on T cell dysfunction. Furthermore, rather than being driven exclusively by specific MDSC subsets such as GPR84-positive cells previously reported [65], this profound senescence program can be triggered by a broader MDSC population through the global remodeling of T cell glucose metabolism. These findings support a shared role for MDSCs as important contributors to the immunometabolic processes associated with T-cell senescence across the sepsis and tumor models.

In fact, a central issue in senescence biology is understanding how disrupted energy metabolism is transduced into stable cellular senescence signaling. In this study, we delineate a specific signaling pathway mediated by the AMPK-Foxo1 axis under the glucose-deprived conditions enforced by MDSCs. Although *in vivo* AMPK activation reflects a composite of systemic stresses, including inflammatory signaling, mitochondrial dysfunction, hypoxia, and nutrient deprivation, the contribution of MDSC-associated glucose deprivation to this cascade is supported by the broader experimental framework rather than by p-AMPK alone. Intriguingly, while AMPK is widely recognized as an anti-senescence kinase that preserves energy homeostasis primarily by promoting fatty acid oxidation and mitochondrial biogenesis in most cell types [66-68], emerging evidence from T cell studies including the present work reveal a paradoxical pro-senescent function under severe nutrient stress. This contradiction likely arises from the specific metabolic profile of effector T cells. Specifically, upon activation, effector T cells undergo massive metabolic reprogramming, becoming heavily reliant on aerobic glycolysis and the PPP to meet the high bioenergetic and biosynthetic demands of clonal expansion and effector functions. This specialized profile leaves them with limited metabolic plasticity [15, 21, 69-73]. Unlike other cell types, when faced with sustained glucose deprivation, T cells fail to engage alternative bioenergetic routes like fatty acid oxidation effectively [74, 75]. Under these conditions, AMPK remains constitutively active as an energy sensor, yet its homeostatic potential is compromised by substrate shortage. Instead, it recruits Foxo1 to initiate an emergency transcriptional program, prioritizing immediate survival via cell-cycle arrest at the cost of long-term dysfunction. This reinforces a context-dependent "AMPK-senescence" paradigm where AMPK acts as a pro-senescent checkpoint in metabolically vulnerable T cells. Consequently, pharmacological inhibition might exert stronger effects on these metabolically stressed T cells, reflecting a differential pathway dependency.

Importantly, our study identifies the impairment of PPP metabolic capacity as another key mechanism underlying MDSC-induced T cell senescence. As the primary cytosolic source of NADPH, a functional PPP is essential for maintaining the glutathione pool and scavenging ROS [58]. Accumulating evidence highlights the central role of the PPP and NADPH in the fate decision and effector function of immune cells, including T cell proliferation, survival, and resistance to activation-induced apoptosis [76], as well as macrophage redox balance and inflammatory programming [77-79]. Of note, enhanced PPP activity is associated with prolonged lifespan and oxidative stress resistance in model organisms [80], whereas its impairment is connected to tissue senescence and degenerative diseases in mammals [81]. We

demonstrate that MDSC-mediated glucose sequestration significantly restricts PPP metabolic capacity, leading to NADPH depletion and exacerbated oxidative stress. Furthermore, transcriptomic analysis revealed a concurrent downregulation of glutamine influx and glutaminolysis enzymes in MDSC-exposed T cells. This impairment may restrict GSH biosynthesis, which together with PPP-driven NADPH depletion to further compromise cellular antioxidant defenses, a synergistic failure supported by the senescence-rescuing effect of exogenous glutamine. This integrated redox failure likely precipitates severe downstream macromolecular damage, cooperating with lipid metabolic remodeling, a recognized parallel driver of T cell senescence [25, 36], to enforce a comprehensive metabolic dysfunction. Thus, the PPP acts as a metabolic hub that translates environmental nutrient scarcity into functional reprogramming. Notably, our imaging flow cytometry analysis demonstrated robust nuclear colocalization between key components of these dual metabolic axes, implying molecular crosstalk between bioenergetic stress and oxidative pressure. This integration may involve potential crosstalk between the two pathways. Specifically, persistent AMPK activation prioritizes survival by suppressing anabolic flux [82], which may further restrict the entry of residual glucose into the PPP. Concurrently, the oxidative stress resulting from PPP deficiency triggers a sustained ATM-dependent DDR [83]. Given that ATM has been reported to directly activate AMPK in other contexts [84], these pathways might cooperate to maintain the senescence-associated program. However, these inferences require further validation through bidirectional pathway-intervention experiments.

From a therapeutic perspective, we evaluated the potential benefits of combining anti-senescence interventions with ICB therapy in the B16F10 melanoma model. Our findings indicate that PD-L1 antibody therapy, when combined with interventions, including NADPH supplementation, depletion of myeloid cells, and pharmacological inhibition of ATM signaling, significantly increases both the quantity and effector function of tumor-infiltrating T cells, thereby improving tumor control in the B16F10 melanoma model. These combination effects may reflect the differences in the biological features of senescence- and exhaustion-associated T cell dysfunction, despite the partial phenotypic overlap between these states [10]. Our integrated RNA-seq and ATAC-seq analyses revealed that MDSC-induced senescent T cells exhibit a chromatin landscape enriched for SASP-related genes and cell-cycle regulator genes, representing a predominant phenotype functionally consistent with senescence [85-87]. While immune exhaustion represents a progressive loss of effector function that is partially reversible through PD-1/PD-L1 blockade, senescence is characterized by cell-cycle arrest, accompanied by metabolic shifts and altered chromatin accessibility, which may limit the response to current

checkpoint therapies. Consequently, simultaneously targeting senescence and the PD-1/PD-L1 axis addresses different but partially overlapping mechanisms contributing to T cell dysfunction, thereby broadening a multidimensional reshaping of antitumor immunity. Furthermore, considering that ICB monotherapy can induce immune-related adverse events [88, 89], whether these combination strategies influence treatment-related toxicity remains to be investigated.

This study extends the MDSC-metabolic-senescence axis from tumor biology to infection, highlighting its broader significance across divergent disease models [90-94]. While previous studies have linked sepsis to premature T cell senescence and thymic atrophy, the underlying mechanism remains poorly understood [2, 95]. Our findings support a potential contribution of MDSC-associated metabolic competition. Initially, the onset of T cell senescence is a consequence of the severe infectious insult, which rapidly mobilizes MDSCs to enforce metabolic starvation. However, these senescent T cells may contribute to subsequent disease pathogenesis once established. During the acute hyperinflammatory phase, these cells may contribute to inflammatory amplification through the SASP, whereas their persistence may contribute to later immune dysfunction through loss of functional effector capacity. This temporal dynamic provides a potential mechanistic explanation for the concurrent hyperinflammation and immunosuppression observed in septic patients. Importantly, we demonstrate that systemic pharmacological interventions targeting these metabolic and senescence-associated pathways in septic mice effectively dampen inflammatory cytokines, reduce tissue damage, restore T cell function, and improve survival. Therefore, these systemic interventions may offer a potential dual benefit by suppressing excessive inflammation and alleviating T-cell dysfunction. However, this macroscopic survival benefit must be interpreted cautiously. Given the overlapping surface markers, anti-Gr1/anti-Ly6G-mediated depletion strategies inevitably compromise both MDSCs and mature neutrophils *in vivo*. Importantly, as sepsis survival is jointly determined by infection control, host inflammation, organ injury, and immune recovery, the observed survival benefit is likely a net macroscopic result of targeting the broader $Gr1^{+}/Ly6G^{+}$ myeloid cells. This benefit may result from both alleviation of MDSC-mediated T cell senescence and attenuation of excessive neutrophil-mediated inflammation. The precise *in vivo* causality of MDSC-specific contributions cannot be fully uncoupled by current pharmacological or antibody interventions, which warrants future investigation using MDSC-targeted genetic approaches.

Several limitations of this study should be acknowledged. First, because our *in vivo* pharmacological and metabolic interventions were administered systemically, potential direct effects on other immune or stromal cell types, as well as indirect systemic outcomes, cannot be

completely excluded. Additionally, cell-type- and state-specific genetic models remain necessary for demonstration of senescent T-cell specificity. MDSC-specific genetic manipulation of *Slc2a1* or *Hk2*, together with T cell-specific manipulation of AMPK, *Foxo1*, or ATM-related signaling and the development of cell-targeted drug-delivery strategies, would help clarify the *in vivo* role of MDSC-driven glucose deprivation in regulating T-cell signaling. Second, our *in vitro* studies used the total $CD11b^{+}Gr1^{+}$ MDSC population without separately evaluating PMN-MDSCs and M-MDSCs. Although both subsets showed enhanced glucose-related metabolic activity, their relative contributions to metabolic competition and T cell senescence remain to be determined. Finally, due to the lack of *in vivo* lineage-tracing, long-term fate mapping, or long-term restimulation models, the long-term stability and irreversibility of this senescent state were not tested, and the long-term fate of these T cells within the tissue microenvironment cannot be definitively established.

In summary, this study elucidates the mechanism by which MDSCs drive T cell senescence through glucose competition and the resulting dual energy and oxidative stress. By clarifying the roles of AMPK-Foxo1 and PPP-redox axes, we provide a mechanistic blueprint for the metabolic regulation of immunosenescence. More importantly, these findings suggest that the MDSC-metabolic-senescence axis may represent a shared immunometabolic feature in mouse models of tumor and sepsis, providing potential targets for therapeutic intervention. Future investigations into how these metabolic cues are translated into long-term epigenetic memory will be crucial for refining therapeutic strategies across a broader range of human diseases.

Acknowledgements

This study was supported by the National Natural Science Foundation of China (82171548, 82471585 and 82274479), Beijing Municipal Administration of hospitals' Ascent Plan (DFL20241802), and High-Level Public Health Specialized Talents Project of Beijing Municipal Health Commission (2022-02-27). We thank Yufei Chang for assistance with patient recruitment.

Author contributions

QYP and JYY performed the experiments, analyzed the data, and drafted the manuscript. MZ, MQJ, XYW, and YJL performed the experiments. ZYY critically reviewed the manuscript. YXK and QYP designed the study, analyzed the data, and revised the manuscript. All authors read and approved the final version of the manuscript.

Data availability

The bulk RNA-seq and ATAC-seq data generated in this study have been deposited in the Genome Sequence Archive (GSA) of the National Genomics Data Center (NGDC), China National Center for Bioinformatics, under the BioProject accession number PRJCA055393.

References

1. Sun L, Su Y, Jiao A, Wang X, Zhang B: T cells in health and disease. *Signal transduction and targeted therapy* 2023, 8(1):235.
2. Xu L, Wei C, Chen Y, Wu Y, Shou X, Chen W, Lu D, Sun H, Li W, Yu B *et al*: IL-33 induces thymic involution-associated naive T cell aging and impairs host control of severe infection. *Nature communications* 2022, 13(1):6881.
3. Kalaora S, Nagler A, Wargo JA, Samuels Y: Mechanisms of immune activation and regulation: lessons from melanoma. *Nature reviews Cancer* 2022, 22(4):195-207.
4. Lian J, Yue Y, Yu W, Zhang Y: Immunosenescence: a key player in cancer development. *Journal of hematology & oncology* 2020, 13(1):151.
5. Akbar AN, Henson SM, Lanna A: Senescence of T Lymphocytes: Implications for Enhancing Human Immunity. *Trends in immunology* 2016, 37(12):866-876.
6. Møller SH, Hsueh PC, Yu YR, Zhang L, Ho PC: Metabolic programs tailor T cell immunity in viral infection, cancer, and aging. *Cell metabolism* 2022, 34(3):378-395.
7. Liu Z, Liang Q, Ren Y, Guo C, Ge X, Wang L, Cheng Q, Luo P, Zhang Y, Han X: Immunosenescence: molecular mechanisms and diseases. *Signal transduction and targeted therapy* 2023, 8(1):200.
8. Carrasco E, Gómez de Las Heras MM, Gabandé-Rodríguez E, Desdín-Micó G, Aranda JF, Mittelbrunn M: The role of T cells in age-related diseases. *Nature reviews Immunology* 2022, 22(2):97-111.
9. Xu W, Larbi A: Markers of T Cell Senescence in Humans. *International journal of molecular sciences* 2017, 18(8).
10. Zhao Y, Shao Q, Peng G: Exhaustion and senescence: two crucial dysfunctional states of T cells in the tumor microenvironment. *Cellular & molecular immunology* 2020, 17(1):27-35.
11. Davalos AR, Coppe JP, Campisi J, Desprez PY: Senescent cells as a source of inflammatory factors for tumor progression. *Cancer metastasis reviews* 2010, 29(2):273-283.
12. Xu X, Wei F, Xiao L, Wu R, Wei B, Huang S, Yi J, Cui W: High proportion of circulating CD8 + CD28- senescent T cells is an independent predictor of distant metastasis in nasopharyngeal canrcinoma after radiotherapy. *Journal of translational medicine* 2023, 21(1):64.
13. Chen ACY, Jaiswal S, Martinez D, Yerinde C, Ji K, Miranda V, Fung ME, Weiss SA, Zschummel M, Taguchi K *et al*: The aged tumor microenvironment limits T cell control

of cancer. *Nature immunology* 2024, 25(6):1033-1045.

14. Covre LP, De Maeyer RPH, Gomes DCO, Akbar AN: The role of senescent T cells in immunopathology. *Aging cell* 2020, 19(12):e13272.

15. Chang CH, Curtis JD, Maggi LB, Jr., Faubert B, Villarino AV, O'Sullivan D, Huang SC, van der Windt GJ, Blagih J, Qiu J *et al*: Posttranscriptional control of T cell effector function by aerobic glycolysis. *Cell* 2013, 153(6):1239-1251.

16. Patsoukis N, Bardhan K, Chatterjee P, Sari D, Liu B, Bell LN, Karoly ED, Freeman GJ, Petkova V, Seth P *et al*: PD-1 alters T-cell metabolic reprogramming by inhibiting glycolysis and promoting lipolysis and fatty acid oxidation. *Nature communications* 2015, 6:6692.

17. Ho PC, Bihuniak JD, Macintyre AN, Staron M, Liu X, Amezquita R, Tsui YC, Cui G, Micevic G, Perales JC *et al*: Phosphoenolpyruvate Is a Metabolic Checkpoint of Anti-tumor T Cell Responses. *Cell* 2015, 162(6):1217-1228.

18. Carr EL, Kelman A, Wu GS, Gopaul R, Senkevitch E, Aghvanyan A, Turay AM, Frauwirth KA: Glutamine uptake and metabolism are coordinately regulated by ERK/MAPK during T lymphocyte activation. *Journal of immunology (Baltimore, Md : 1950)* 2010, 185(2):1037-1044.

19. Johnson MO, Wolf MM, Madden MZ, Andrejeva G, Sugiura A, Contreras DC, Maseda D, Liberti MV, Paz K, Kishton RJ *et al*: Distinct Regulation of Th17 and Th1 Cell Differentiation by Glutaminase-Dependent Metabolism. *Cell* 2018, 175(7):1780-1795.e1719.

20. Reinfeld BI, Madden MZ, Wolf MM, Chytil A, Bader JE, Patterson AR, Sugiura A, Cohen AS, Ali A, Do BT *et al*: Cell-programmed nutrient partitioning in the tumour microenvironment. *Nature* 2021, 593(7858):282-288.

21. Chang CH, Qiu J, O'Sullivan D, Buck MD, Noguchi T, Curtis JD, Chen Q, Gindin M, Gubin MM, van der Windt GJ *et al*: Metabolic Competition in the Tumor Microenvironment Is a Driver of Cancer Progression. *Cell* 2015, 162(6):1229-1241.

22. Liu X, Mo W, Ye J, Li L, Zhang Y, Hsueh EC, Hoft DF, Peng G: Regulatory T cells trigger effector T cell DNA damage and senescence caused by metabolic competition. *Nature communications* 2018, 9(1):249.

23. Ye J, Ma C, Hsueh EC, Dou J, Mo W, Liu S, Han B, Huang Y, Zhang Y, Varvares MA *et al*: TLR8 signaling enhances tumor immunity by preventing tumor-induced T cell senescence. *EMBO molecular medicine* 2014, 6(10):1294-1311.

24. Ye J, Peng G: Controlling T cell senescence in the tumor microenvironment for tumor

immunotherapy. *Oncoimmunology* 2015, 4(3):e994398.

25. Ma F, Liu X, Zhang Y, Tao Y, Zhao L, Abusalamah H, Huffman C, Harbison RA, Puram SV, Wang Y *et al*: Tumor extracellular vesicle-derived PD-L1 promotes T cell senescence through lipid metabolism reprogramming. *Science translational medicine* 2025, 17(785):eadm7269.

26. Gao A, Liu X, Lin W, Wang J, Wang S, Si F, Huang L, Zhao Y, Sun Y, Peng G: Tumor-derived ILT4 induces T cell senescence and suppresses tumor immunity. *Journal for immunotherapy of cancer* 2021, 9(3).

27. Hotchkiss RS, Monneret G, Payen D: Sepsis-induced immunosuppression: from cellular dysfunctions to immunotherapy. *Nature reviews Immunology* 2013, 13(12):862-874.

28. Hotchkiss RS, Osmon SB, Chang KC, Wagner TH, Coopersmith CM, Karl IE: Accelerated lymphocyte death in sepsis occurs by both the death receptor and mitochondrial pathways. *Journal of immunology (Baltimore, Md : 1950)* 2005, 174(8):5110-5118.

29. Wu Y, Yi M, Niu M, Mei Q, Wu K: Myeloid-derived suppressor cells: an emerging target for anticancer immunotherapy. *Molecular cancer* 2022, 21(1):184.

30. Deng Y, Yang J, Luo F, Qian J, Liu R, Zhang D, Yu H, Chu Y: mTOR-mediated glycolysis contributes to the enhanced suppressive function of murine tumor-infiltrating monocytic myeloid-derived suppressor cells. *Cancer immunology, immunotherapy : CII* 2018, 67(9):1355-1364.

31. Hossain F, Al-Khami AA, Wyczechowska D, Hernandez C, Zheng L, Reiss K, Valle LD, Trillo-Tinoco J, Maj T, Zou W *et al*: Inhibition of Fatty Acid Oxidation Modulates Immunosuppressive Functions of Myeloid-Derived Suppressor Cells and Enhances Cancer Therapies. *Cancer immunology research* 2015, 3(11):1236-1247.

32. Singer M, Deutschman CS, Seymour CW, Shankar-Hari M, Annane D, Bauer M, Bellomo R, Bernard GR, Chiche JD, Coopersmith CM *et al*: The Third International Consensus Definitions for Sepsis and Septic Shock (Sepsis-3). *Jama* 2016, 315(8):801-810.

33. Marrero JA, Kulik LM, Sirlin CB, Zhu AX, Finn RS, Abecassis MM, Roberts LR, Heimbach JK: Diagnosis, Staging, and Management of Hepatocellular Carcinoma: 2018 Practice Guidance by the American Association for the Study of Liver Diseases. *Hepatology (Baltimore, Md)* 2018, 68(2):723-750.

34. EASL Clinical Practice Guidelines: Management of hepatocellular carcinoma. *Journal*

of hepatology 2018, 69(1):182-236.

35. Yang JM, Zhang N, Luo T, Yang M, Shen WK, Tan ZL, Xia Y, Zhang L, Zhou X, Lei Q *et al*: TCellSI: A novel method for T cell state assessment and its applications in immune environment prediction. *iMeta* 2024, 3(5):e231.

36. Liu X, Hartman CL, Li L, Albert CJ, Si F, Gao A, Huang L, Zhao Y, Lin W, Hsueh EC *et al*: Reprogramming lipid metabolism prevents effector T cell senescence and enhances tumor immunotherapy. *Science translational medicine* 2021, 13(587).

37. Sukiennicki TL, Fowell DJ: Distinct molecular program imposed on CD4+ T cell targets by CD4+CD25+ regulatory T cells. *Journal of immunology (Baltimore, Md : 1950)* 2006, 177(10):6952-6961.

38. Alfei F, Kanev K, Hofmann M, Wu M, Ghoneim HE, Roelli P, Utzschneider DT, von Hoesslin M, Cullen JG, Fan Y *et al*: TOX reinforces the phenotype and longevity of exhausted T cells in chronic viral infection. *Nature* 2019, 571(7764):265-269.

39. Waibl Polania J, Hoyt-Miggelbrink A, Tomaszewski WH, Wachsmuth LP, Lorrey SJ, Wilkinson DS, Lerner E, Woroniecka K, Finlay JB, Ayasoufi K *et al*: Antigen presentation by tumor-associated macrophages drives T cells from a progenitor exhaustion state to terminal exhaustion. *Immunity* 2025, 58(1):232-246.e236.

40. Van Nguyen T, Puebla-Osorio N, Pang H, Dujka ME, Zhu C: DNA damage-induced cellular senescence is sufficient to suppress tumorigenesis: a mouse model. *The Journal of experimental medicine* 2007, 204(6):1453-1461.

41. Rodier F, Coppé JP, Patil CK, Hoeijmakers WA, Muñoz DP, Raza SR, Freund A, Campeau E, Davalos AR, Campisi J: Persistent DNA damage signalling triggers senescence-associated inflammatory cytokine secretion. *Nature cell biology* 2009, 11(8):973-979.

42. Huang L, Zhang C, Jiang A, Lin A, Zhu L, Mou W, Zeng D, Liu Z, Tang B, Zhang J *et al*: T cell senescence in the Tumor Microenvironment. *Cancer immunology research* 2025, 13(5):618-632.

43. Salminen A, Kaarniranta K: AMP-activated protein kinase (AMPK) controls the aging process via an integrated signaling network. *Ageing research reviews* 2012, 11(2):230-241.

44. Lanna A, Henson SM, Escors D, Akbar AN: The kinase p38 activated by the metabolic regulator AMPK and scaffold TAB1 drives the senescence of human T cells. *Nature immunology* 2014, 15(10):965-972.

45. Fu X, Wan S, Lyu YL, Liu LF, Qi H: Etoposide induces ATM-dependent mitochondrial

biogenesis through AMPK activation. *PloS one* 2008, 3(4):e2009.

46. Lanna A, Gomes DC, Muller-Durovic B, McDonnell T, Escors D, Gilroy DW, Lee JH, Karin M, Akbar AN: A sestrin-dependent Erk-Jnk-p38 MAPK activation complex inhibits immunity during aging. *Nature immunology* 2017, 18(3):354-363.

47. Nakamura N, Ramaswamy S, Vazquez F, Signoretti S, Loda M, Sellers WR: Forkhead transcription factors are critical effectors of cell death and cell cycle arrest downstream of PTEN. *Molecular and cellular biology* 2000, 20(23):8969-8982.

48. Ramaswamy S, Nakamura N, Sansal I, Bergeron L, Sellers WR: A novel mechanism of gene regulation and tumor suppression by the transcription factor FKHR. *Cancer cell* 2002, 2(1):81-91.

49. Schmidt M, Fernandez de Mattos S, van der Horst A, Klompmaker R, Kops GJ, Lam EW, Burgering BM, Medema RH: Cell cycle inhibition by FoxO forkhead transcription factors involves downregulation of cyclin D. *Molecular and cellular biology* 2002, 22(22):7842-7852.

50. Tran H, Brunet A, Grenier JM, Datta SR, Fornace AJ, Jr., DiStefano PS, Chiang LW, Greenberg ME: DNA repair pathway stimulated by the forkhead transcription factor FOXO3a through the Gadd45 protein. *Science (New York, NY)* 2002, 296(5567):530-534.

51. Alvarez B, Martínez AC, Burgering BM, Carrera AC: Forkhead transcription factors contribute to execution of the mitotic programme in mammals. *Nature* 2001, 413(6857):744-747.

52. Seoane J, Le HV, Shen L, Anderson SA, Massagué J: Integration of Smad and forkhead pathways in the control of neuroepithelial and glioblastoma cell proliferation. *Cell* 2004, 117(2):211-223.

53. Muñoz-Espín D, Cañamero M, Maraver A, Gómez-López G, Contreras J, Murillo-Cuesta S, Rodríguez-Baeza A, Varela-Nieto I, Ruberte J, Collado M *et al*: Programmed cell senescence during mammalian embryonic development. *Cell* 2013, 155(5):1104-1118.

54. Bae JH, Jeong HJ, Kim H, Leem YE, Ryu D, Park SC, Lee YI, Cho SC, Kang JS: ZNF746/PARIS overexpression induces cellular senescence through FoxO1/p21 axis activation in myoblasts. *Cell death & disease* 2020, 11(5):359.

55. Kundu D, Kennedy L, Zhou T, Ekser B, Meadows V, Sybenga A, Kyritsi K, Chen L, Ceci L, Wu N *et al*: p16 INK4A drives nonalcoholic fatty liver disease phenotypes in high fat diet fed mice through biliary E2F1/FOXO1/IGF-1 signaling. *Hepatology*

(Baltimore, Md) 2023, 78(1):243-257.

56. Rodriguez-Colman MJ, Dansen TB, Burgering BMT: FOXO transcription factors as mediators of stress adaptation. *Nature reviews Molecular cell biology* 2024, 25(1):46-64.

57. Tzivion G, Dobson M, Ramakrishnan G: FoxO transcription factors; Regulation by AKT and 14-3-3 proteins. *Biochimica et biophysica acta* 2011, 1813(11):1938-1945.

58. TeSlaa T, Ralser M, Fan J, Rabinowitz JD: The pentose phosphate pathway in health and disease. *Nature metabolism* 2023, 5(8):1275-1289.

59. Gabrilovich DI: Myeloid-Derived Suppressor Cells. *Cancer immunology research* 2017, 5(1):3-8.

60. Marvel D, Gabrilovich DI: Myeloid-derived suppressor cells in the tumor microenvironment: expect the unexpected. *The Journal of clinical investigation* 2015, 125(9):3356-3364.

61. Ostrand-Rosenberg S, Fenselau C: Myeloid-Derived Suppressor Cells: Immune-Suppressive Cells That Impair Antitumor Immunity and Are Sculpted by Their Environment. *Journal of immunology (Baltimore, Md : 1950)* 2018, 200(2):422-431.

62. Derive M, Bouazza Y, Alauzet C, Gibot S: Myeloid-derived suppressor cells control microbial sepsis. *Intensive care medicine* 2012, 38(6):1040-1049.

63. Brudecki L, Ferguson DA, McCall CE, El Gazzar M: Myeloid-derived suppressor cells evolve during sepsis and can enhance or attenuate the systemic inflammatory response. *Infection and immunity* 2012, 80(6):2026-2034.

64. Ruan WS, Feng MX, Xu J, Xu YG, Song CY, Lin LY, Li L, Lu YQ: Early Activation of Myeloid-Derived Suppressor Cells Participate in Sepsis-Induced Immune Suppression via PD-L1/PD-1 Axis. *Frontiers in immunology* 2020, 11:1299.

65. Liu J, Liu J, Qin G, Li J, Fu Z, Li J, Li M, Guo C, Zhao M, Zhang Z *et al*: MDSCs-derived GPR84 induces CD8(+) T cell senescence via p53 activation to suppress the antitumor response. *Journal for immunotherapy of cancer* 2023, 11(11).

66. Yang L, Wang B, Guo F, Huang R, Liang Y, Li L, Tao S, Yin T, Fu P, Ma L: FFAR4 improves the senescence of tubular epithelial cells by AMPK/SirT3 signaling in acute kidney injury. *Signal transduction and targeted therapy* 2022, 7(1):384.

67. van Vliet T, Varela-Eirin M, Wang B, Borghesan M, Brandenburg SM, Franzin R, Evangelou K, Seelen M, Gorgoulis V, Demaria M: Physiological hypoxia restrains the senescence-associated secretory phenotype via AMPK-mediated mTOR suppression. *Molecular cell* 2021, 81(9):2041-2052.e2046.

68. Campos JC, Marchesi Bozi LH, Krum B, Grassmann Bechara LR, Ferreira ND, Arini GS, Albuquerque RP, Traa A, Ogawa T, van der Bliek AM *et al*: Exercise preserves physical fitness during aging through AMPK and mitochondrial dynamics. *Proceedings of the National Academy of Sciences of the United States of America* 2023, 120(2):e2204750120.
69. Macintyre AN, Gerriets VA, Nichols AG, Michalek RD, Rudolph MC, Deoliveira D, Anderson SM, Abel ED, Chen BJ, Hale LP *et al*: The glucose transporter Glut1 is selectively essential for CD4 T cell activation and effector function. *Cell metabolism* 2014, 20(1):61-72.
70. Michalek RD, Gerriets VA, Jacobs SR, Macintyre AN, MacIver NJ, Mason EF, Sullivan SA, Nichols AG, Rathmell JC: Cutting edge: distinct glycolytic and lipid oxidative metabolic programs are essential for effector and regulatory CD4+ T cell subsets. *Journal of immunology (Baltimore, Md : 1950)* 2011, 186(6):3299-3303.
71. Sinclair LV, Rolf J, Emslie E, Shi YB, Taylor PM, Cantrell DA: Control of amino-acid transport by antigen receptors coordinates the metabolic reprogramming essential for T cell differentiation. *Nature immunology* 2013, 14(5):500-508.
72. Angela M, Endo Y, Asou HK, Yamamoto T, Tumes DJ, Tokuyama H, Yokote K, Nakayama T: Fatty acid metabolic reprogramming via mTOR-mediated inductions of PPARγ directs early activation of T cells. *Nature communications* 2016, 7:13683.
73. Wahl DR, Byersdorfer CA, Ferrara JL, Opipari AW, Jr., Glick GD: Distinct metabolic programs in activated T cells: opportunities for selective immunomodulation. *Immunological reviews* 2012, 249(1):104-115.
74. Manzo T, Prentice BM, Anderson KG, Raman A, Schalck A, Codreanu GS, Nava Lauson CB, Tiberti S, Raimondi A, Jones MA *et al*: Accumulation of long-chain fatty acids in the tumor microenvironment drives dysfunction in intrapancreatic CD8+ T cells. *The Journal of experimental medicine* 2020, 217(8).
75. Hunt EG, Hurst KE, Riesenberg BP, Kennedy AS, Gandy EJ, Andrews AM, Del Mar Alicea Pauneto C, Ball LE, Wallace ED, Gao P *et al*: Acetyl-CoA carboxylase obstructs CD8(+) T cell lipid utilization in the tumor microenvironment. *Cell metabolism* 2024, 36(5):969-983.e910.
76. Chen Z, Olszewski KL, Ryseck RP, Xu X, Boyer JA, Peace CG, Shen Y, Bartman CR, Lynch L, Rabinowitz JD: Oxidative pentose phosphate pathway is required for T cell activation and antitumor immunity. *Proceedings of the National Academy of Sciences of the United States of America* 2025, 122(49):e2516288122.

77. Erlich JR, To EE, Luong R, Liong F, Liong S, Oseghale O, Miles MA, Bozinovski S, Brooks RD, Vlahos R *et al*: Glycolysis and the Pentose Phosphate Pathway Promote LPS-Induced NOX2 Oxidase- and IFN-β-Dependent Inflammation in Macrophages. *Antioxidants (Basel, Switzerland)* 2022, 11(8).
78. Ghergurovich JM, García-Cañaveras JC, Wang J, Schmidt E, Zhang Z, TeSlaa T, Patel H, Chen L, Britt EC, Piqueras-Nebot M *et al*: A small molecule G6PD inhibitor reveals immune dependence on pentose phosphate pathway. *Nature chemical biology* 2020, 16(7):731-739.
79. Britt EC, Lika J, Giese MA, Schoen TJ, Seim GL, Huang Z, Lee PY, Huttenlocher A, Fan J: Switching to the cyclic pentose phosphate pathway powers the oxidative burst in activated neutrophils. *Nature metabolism* 2022, 4(3):389-403.
80. Legan SK, Rebrin I, Mockett RJ, Radyuk SN, Klichko VI, Sohal RS, Orr WC: Overexpression of glucose-6-phosphate dehydrogenase extends the life span of Drosophila melanogaster. *The Journal of biological chemistry* 2008, 283(47):32492-32499.
81. Banki K, Perl A: Cell type-specific regulation of the pentose phosphate pathway during development and metabolic stress-driven autoimmune diseases: Relevance for inflammatory liver, renal, endocrine, cardiovascular and neurobehavioral comorbidities, carcinogenesis, and aging. *Autoimmunity reviews* 2025, 24(5):103781.
82. Trefts E, Shaw RJ: AMPK: restoring metabolic homeostasis over space and time. *Molecular cell* 2021, 81(18):3677-3690.
83. Srinivas US, Tan BWQ, Vellayappan BA, Jeyasekharan AD: ROS and the DNA damage response in cancer. *Redox biology* 2019, 25:101084.
84. Gupta S, Panda PK: An ATM-AMPK-Wip1 feedback loop governing DNA-damage signaling and tumor stress responses. *Cell death & disease* 2026, 17(1).
85. Hao X, Wang C, Zhang R: Chromatin basis of the senescence-associated secretory phenotype. *Trends in cell biology* 2022, 32(6):513-526.
86. Seo H, Chen J, González-Avalos E, Samaniego-Castruita D, Das A, Wang YH, López-Moyado IF, Georges RO, Zhang W, Onodera A *et al*: TOX and TOX2 transcription factors cooperate with NR4A transcription factors to impose CD8(+) T cell exhaustion. *Proceedings of the National Academy of Sciences of the United States of America* 2019, 116(25):12410-12415.
87. Chen C, Liu J, Chen Y, Lin A, Mou W, Zhu L, Yang T, Cheng Q, Zhang J, Luo P: Application of ATAC-seq in tumor-specific T cell exhaustion. *Cancer gene therapy*

2023, 30(1):1-10.

88. Postow MA, Sidlow R, Hellmann MD: Immune-Related Adverse Events Associated with Immune Checkpoint Blockade. *The New England journal of medicine* 2018, 378(2):158-168.

89. Ramos-Casals M, Brahmer JR, Callahan MK, Flores-Chávez A, Keegan N, Khamashta MA, Lambotte O, Mariette X, Prat A, Suárez-Almazor ME: Immune-related adverse events of checkpoint inhibitors. *Nature reviews Disease primers* 2020, 6(1):38.

90. Schrijver IT, Théroude C, Roger T: Myeloid-Derived Suppressor Cells in Sepsis. *Frontiers in immunology* 2019, 10:327.

91. Malavika M, Sanju S, Poorna MR, Vishnu Priya V, Sidharthan N, Varma P, Mony U: Role of myeloid derived suppressor cells in sepsis. *International immunopharmacology* 2022, 104:108452.

92. Macatangay BJ, Landay AL, Rinaldo CR: MDSC: a new player in HIV immunopathogenesis. *AIDS (London, England)* 2012, 26(12):1567-1569.

93. Jøntvedt Jørgensen M, Jenum S, Tonby K, Mortensen R, Walzl G, Du Plessis N, Dyrhol-Riise AM: Monocytic myeloid-derived suppressor cells reflect tuberculosis severity and are influenced by cyclooxygenase-2 inhibitors. *Journal of leukocyte biology* 2021, 110(1):177-186.

94. Rajabinejad M, Salari F, Gorgin Karaji A, Rezaiemanesh A: The role of myeloid-derived suppressor cells in the pathogenesis of rheumatoid arthritis; anti- or pro-inflammatory cells? *Artificial cells, nanomedicine, and biotechnology* 2019, 47(1):4149-4158.

95. Sun H, Hong Q, Li C, Zhu S, Yu Y, Zhang H, Guo K: Immunosenescence in Sepsis: Molecular Mechanisms and Potential Therapeutic Targets. *Aging and disease* 2025, 17(2):780-811.

Figures and Figure legends

Figure 1

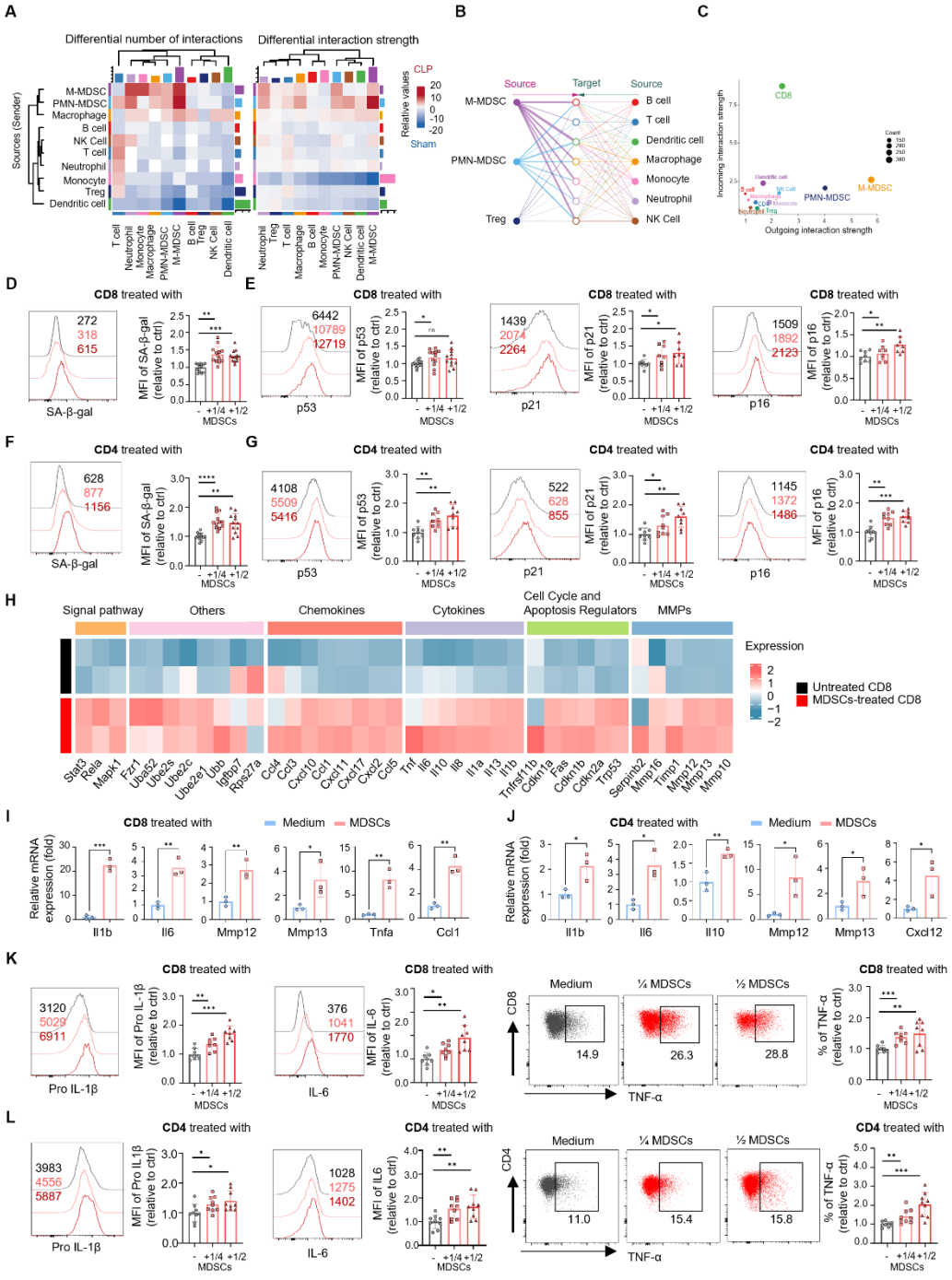


Fig. 1. MDSCs induce T cell senescence and SASP production. A, scRNA-seq CellChat analysis of differential number and strength of interactions between immune cell subsets and relative value within each cell-cell interaction between CLP (red) and Sham (blue). GSE249975, Peritoneal and spleen tissues from CLP and sham mice. **B,** scRNA-seq CellChat hierarchical network consisting of three parts, in which edge thickness indicates interaction strength; the

left panel shows selected cell subsets as signaling senders, the middle panel shows the remaining cell subsets (excluding those on the left) as signaling receivers, and the right panel shows the same subsets as signaling senders. **C,** scRNA-seq CellChat two-dimensional visualization of major signaling sources (outgoing) and targets (incoming). **D-G,** Flow cytometry analysis of SA-β-gal positivity and p53, p21, and p16 expression in $CD8^+$ and $CD4^+$ T cells derived from naïve cells cultured alone or cocultured with MDSCs for 3 days (n= 8-13 independent experiments). **H,** RNA-seq heatmap of SASP-related gene expression in $CD8^+$ T cells derived from naïve cells cultured alone or cocultured with MDSCs for 3 days (n = 2 independent experiments). **I,J,** qRT-PCR analysis of SASP-related gene expression in $CD8^+$ (I) and $CD4^+$ (J) T cells derived from naïve cells cultured alone or cocultured with MDSCs for 3 days (n = 3 independent experiments). **K,L,** Flow cytometry analysis of pro-IL1β, IL6, and TNF-α expression in $CD8^+$ (K) and $CD4^+$ (L) T cells derived from naïve cells cultured alone or cocultured with MDSCs (n = 8 independent experiments). Data are presented as mean ± s.d. Statistical significance in D – G and I – L was assessed using an unpaired two-tailed Student's t-test. *P < 0.05, **P < 0.01, ***P < 0.001, ****P < 0.0001; ns, not significant.

Figure 2

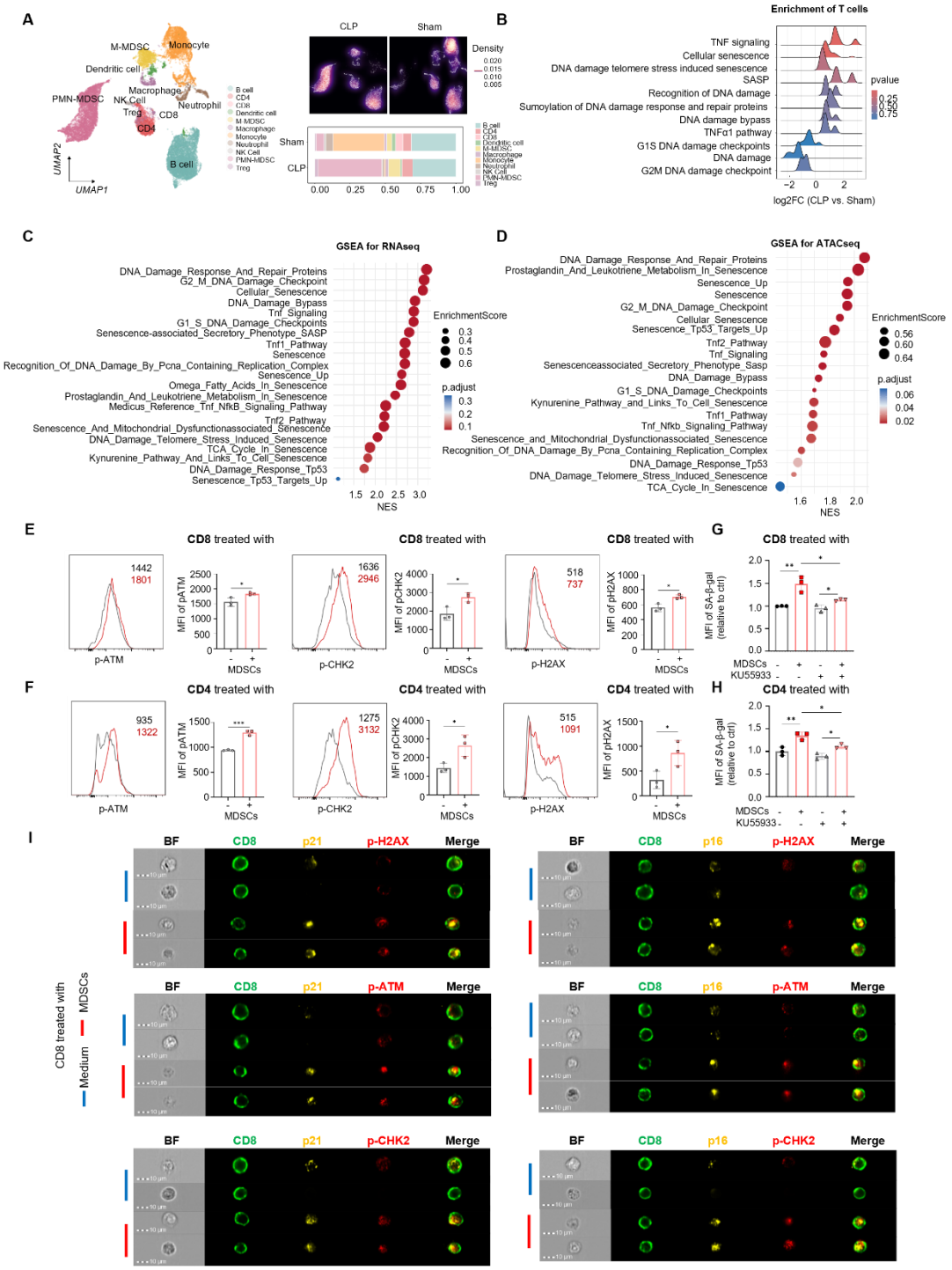


Fig. 2. MDSCs promote T cell senescence and cell-cycle arrest through an ATM-dependent DDR. A, UMAP projection based on scRNA-seq data of cells from a mouse CLP sepsis model, showing the distribution and relative proportions of distinct cell subpopulations. GSE249975, peritoneal and spleen tissues from CLP and sham mice. **B,** Enrichment analysis of senescence- and DNA damage-related gene sets in T cells of CLP versus sham mice. GSE249975, peritoneal

and spleen tissues from CLP and sham mice. **C,** GSEA of senescence- and DNA damage-related gene sets based on RNA-seq data from $CD8^+$ T cells derived from naïve cells cultured alone or cocultured with MDSCs for 3 days. **D,** GSEA of senescence- and DNA damage-related gene sets based on ATAC-seq data from $CD8^+$ T cells derived from naïve cells cultured alone or cocultured with MDSCs for 3 days. **E,F,** Flow cytometry analysis of p-ATM, p-H2AX, and p-CHK2 expression in $CD8^+$ (**E**) and $CD4^+$ (**F**) T cells derived from naïve cells cultured alone or cocultured with MDSCs for 3 days (n = 3 independent experiments). **G,H,** Flow cytometric analysis of SA-β-gal activity in $CD8^+$ (**G**) and $CD4^+$ (**H**) T cells derived from naïve cells pretreated with the ATM inhibitor KU55933 (10 μM) for 24 h, followed by culture alone or coculture with MDSCs for 3 days (n = 3 independent experiments). **I,** Imaging flow cytometry analysis of colocalization between p-ATM, p-H2AX, or p-CHK2 and p16 or p21. Data are presented as mean ± s.d. P values for GSEA enrichment analyses in C–D were adjusted using the Benjamini–Hochberg procedure; data in E,F were analyzed using an unpaired two-tailed Student's t-test, and data in G,H using one-way ANOVA followed by Dunnett's multiple-comparisons test. *P < 0.05, **P < 0.01, ***P < 0.001, ****P < 0.0001; ns, not significant.

Figure 3

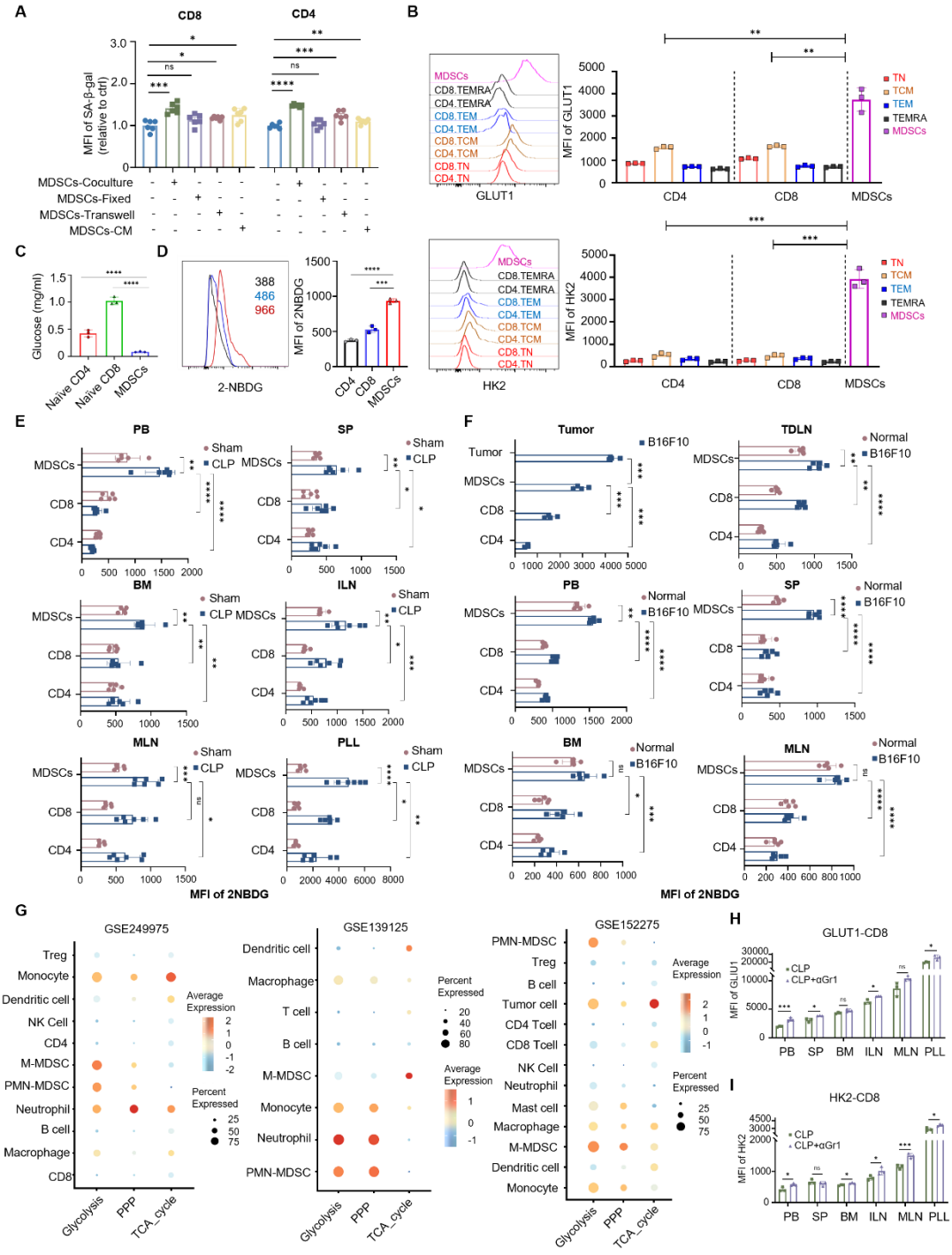


Fig. 3. Metabolic competition for glucose by MDSCs impairs T cell metabolic capacity in sepsis and tumor microenvironments. A, Flow cytometric analysis of SA-β-gal activity in $CD8^+$ and $CD4^+$ T cells derived from naïve cells cultured for 3 days under conditions of direct contact with MDSCs, indirect coculture with MDSCs via transwell, coculture with fixed MDSCs, or culture in MDSC-conditioned medium (n = 6 independent experiments). **B,** Flow cytometric analysis of GLUT1 and HK2 expression in MDSCs and T cell subsets, including

naïve T cells (TN), central memory T cells (TCM), effector memory T cells (TEM), and terminally differentiated effector memory T cells (TEMRA), in the peripheral blood of septic mice (n = 3 mice). TN, $CD44^{-}CD62L^{+}$; TCM, $CD44^{+}CD62L^{+}$; TEM, $CD44^{+}CD62L^{-}$; TEMRA, $CD44^{-}CD62L^{-}$. **C,** Quantification of residual glucose levels in culture medium after 3 days of independent culture of equal numbers of naïve T cells or MDSCs (n = 3 independent experiments). **D,** Flow cytometry analysis of 2-NBDG uptake in $CD4^{+}$ or $CD8^{+}$ T cells derived from naïve cells, as well as in MDSCs, after 3 days of coculture (n = 3 independent experiments). **E,F,** Flow cytometry analysis of 2-NBDG uptake by MDSCs and T cells from multiple tissues 1 h after tail vein injection of 2-NBDG in CLP and sham (**E**) or B16F10 tumor-bearing and normal (**F**) mice (n = 5-6 mice per group). PB, peripheral blood; SP, spleen; BM, bone marrow; ILN, inguinal lymph node; MLN, mesenteric lymph node; PLL, peritoneal lavage fluid; TDLN, tumor-draining lymph node. **G,** Dot plot based on scRNA-seq data showing metabolic features of glycolysis, the pentose phosphate pathway, and the TCA cycle across distinct cell subpopulations. GSE249975, Peritoneal and spleen tissues from CLP and sham mice ; GSE139125, Spleen tissues from breast cancer and normal mice; GSE152275, Tumor tissues from glioma mice. **H,I**, Flow cytometry analysis of GLUT1 (**H**) and HK2 (**I**) expression in $CD8^{+}$ T cells from multiple tissues of CLP mice treated with vehicle or the anti-Gr1 antibody (n = 3 mice per group). PB, peripheral blood; SP, spleen; BM, bone marrow; ILN, inguinal lymph node; MLN, mesenteric lymph node; PLL, peritoneal lavage fluid. Data are presented as mean ± s.d. Data in A–D were analyzed using one-way ANOVA followed by Tukey's multiple-comparisons test, whereas data in E,F,H,I were analyzed using two-way repeated-measures ANOVA followed by Šídák's multiple-comparisons test. *P < 0.05, **P < 0.01, ***P < 0.001, ****P < 0.0001; ns, not significant.

Figure 4

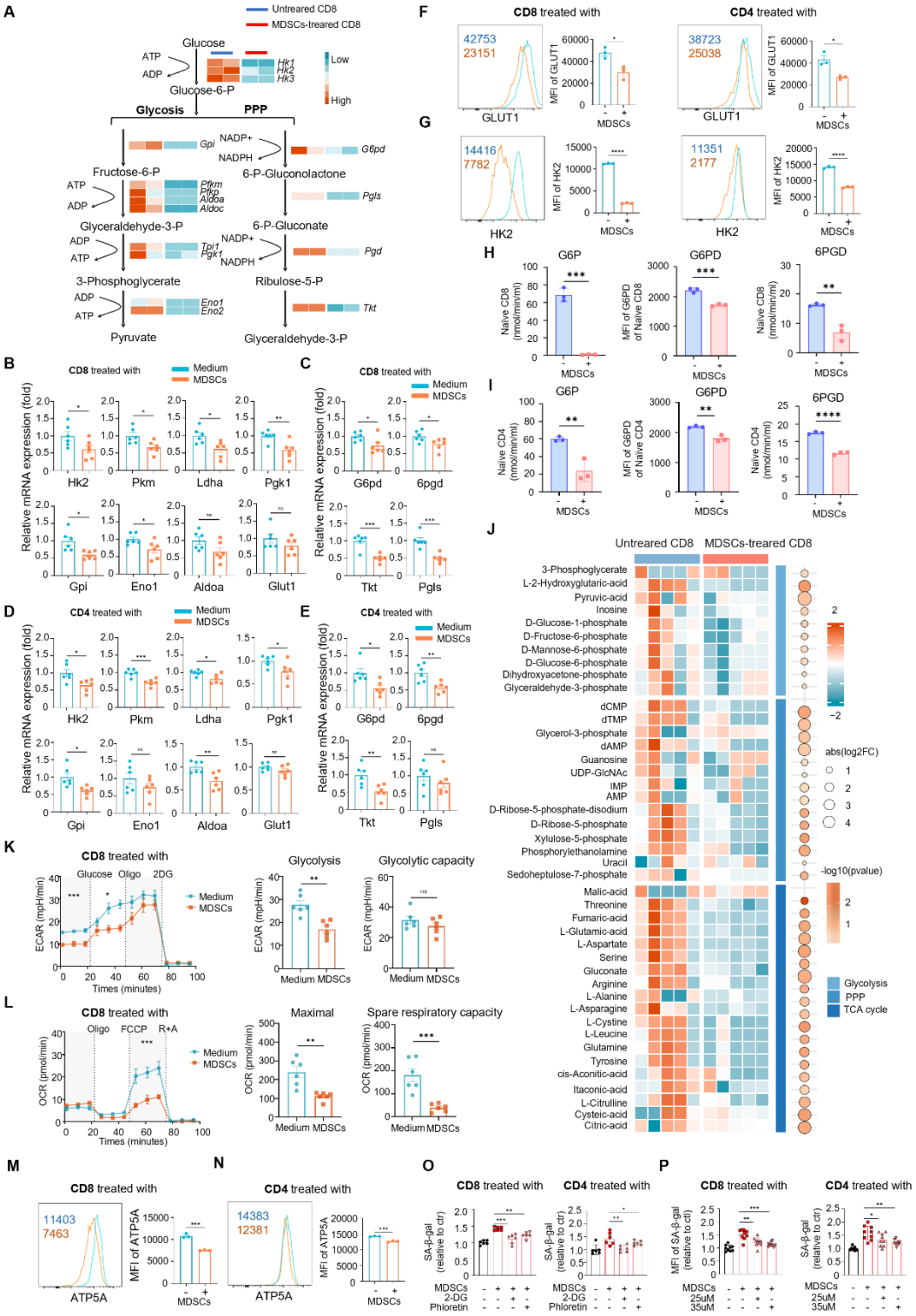


Fig. 4. MDSCs drive T cell senescence by reprogramming glucose metabolism and bioenergetic fitness. A, RNA-seq heatmap of glycolysis- and pentose phosphate pathway-related gene expression in CD8$^+$ T cells derived from naïve cells cultured alone or cocultured with MDSCs for 3 days (n = 2 independent experiments). **B-E,** qRT-PCR analysis of glycolysis- and PPP-related gene expression in CD8$^+$ (**B,C**) and CD4$^+$ (**D,E**) T cells derived from naïve

cells cultured alone or cocultured with MDSCs for 3 days (n = 6 independent experiments). **F,G,** Flow cytometry analysis of GLUT1 (**F**) and HK2 (**G**) expression in $CD8^+$ and $CD4^+$ T cells derived from naïve cells cultured alone or cocultured with MDSCs for 3 days (n = 3 independent experiments). **H,I,** Quantification of G6P and 6PGD activity and flow cytometry analysis of G6PD expression in $CD8^+$ (H) and $CD4^+$ (I) T cells derived from naïve cells cultured alone or cocultured with MDSCs for 3 days (n = 3 independent experiments). **J,** Heatmap of the relative abundance of energy metabolism-related metabolites in $CD8^+$ T cells derived from naïve cells cultured alone or cocultured with MDSCs for 3 days (n = 5 independent experiments). **K,** ECAR of $CD8^+$ T cells derived from naïve cells cultured alone or cocultured with MDSCs, measured using a Seahorse extracellular flux analyzer (n = 6 independent experiments). **L**, OCR of $CD8^+$ T cells derived from naïve cells cultured alone or cocultured with MDSCs, measured using a Seahorse extracellular flux analyzer (n = 6 independent experiments). **M,N,** Flow cytometry analysis of ATP5A expression in $CD8^+$ (**M**) and $CD4^+$ (**N**) T cells derived from naïve cells cultured alone or cocultured with MDSCs for 3 days (n = 3 independent experiments). **O,** Flow cytometry analysis of SA-β-gal activity in $CD8^+$ and $CD4^+$ T cells derived from naïve cells cocultured with MDSCs for 3 days, with MDSCs pretreated for 24 h with the glucose metabolism inhibitor phloretin (2 μM) or 2-DG (1 mM) (n = 9 independent experiments). **P,** Flow cytometry analysis of SA-β-gal activity in $CD8^+$ and $CD4^+$ T cells derived from naïve cells cocultured with MDSCs for 3 days, with additional glucose supplementation (25 μM and 35 μM) (n = 9 independent experiments). Data in B–I and M,N were analyzed using an unpaired two-tailed Student's t-test; time-course data in K,L were analyzed using two-way ANOVA followed by Šídák's multiple-comparisons test, and data in O,P using one-way ANOVA followed by Dunnett's multiple-comparisons test. Data are presented as mean ± s.d. *P < 0.05, **P < 0.01, ***P < 0.001, ****P < 0.0001; ns, not significant.

Figure 5

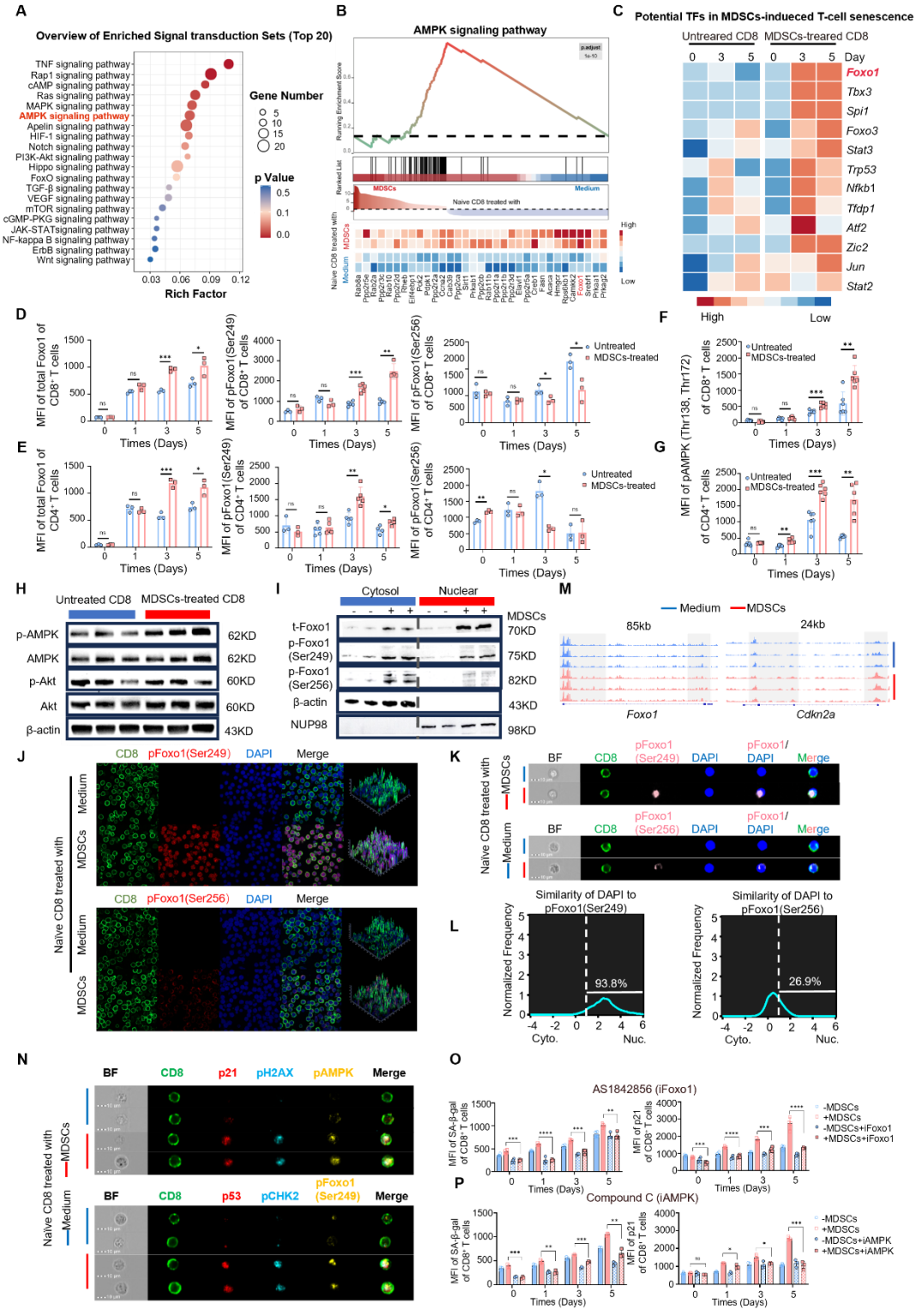


Fig. 5. Activation of the AMPK-Foxo1 signaling axis contributes to MDSC-mediated T cell senescence. A, KEGG enrichment analysis of signaling pathways in senescent CD8⁺ T cells after 3 days of coculture with MDSCs. **B,** GSEA and gene expression heatmap of AMPK signaling pathway-related genes in senescent CD8⁺ T cells after 3 days of coculture with

MDSCs. **C,** Heatmap of transcription factor expression changes in $CD8^+$ T cells during MDSC-induced senescence. **D,E,** Flow cytometry analysis of Foxo1, p-Foxo1 (Ser249), and p-Foxo1 (Ser256) expression in $CD8^+$ (**D**) and $CD4^+$ (**E**) T cells derived from naïve cells cultured alone or cocultured with MDSCs at indicated time points (n = 3-5 independent experiments). **F,G,** Flow cytometry analysis of AMPK phosphorylation in $CD8^+$ (**F**) and $CD4^+$ (**G**) T cells derived from naïve cells cultured alone or cocultured with MDSCs at indicated time points (n = 6 independent experiments). **H,** Western blot analysis of total and phosphorylated AMPK and AKT in $CD8^+$ T cells derived from naïve cells cultured alone or cocultured with MDSCs for 3 days. **I,** Western blot analysis of Foxo1 and its phosphorylated forms in cytoplasmic and nuclear fractions of $CD8^+$ T cells derived from naïve cells cultured alone or cocultured with MDSCs for 3 days. **J,** Confocal immunofluorescence analysis of the subcellular localization of phosphorylated Foxo1 in $CD8^+$ T cells derived from naïve cells cultured alone or cocultured with MDSCs for 3 days. **K,L,** Imaging flow cytometry analysis of the intracellular localization of p-Foxo1 (Ser249) and p-Foxo1 (Ser256) in $CD8^+$ T cells derived from naïve cells cultured alone or cocultured with MDSCs for 3 days. **M,** ATAC-seq peak plots of chromatin accessibility at the *Foxo1* and *Cdkn2a* gene in $CD8^+$ T cells derived from naïve cells cultured alone or cocultured with MDSCs for 3 days (n = 3 independent experiments). **N,** Imaging flow cytometry analysis of colocalization between p-H2AX or p-CHK2 and p-AMPK or p-Foxo1 (Ser249), as well as with p53 or p21 in $CD8^+$ T cells derived from naïve cells cultured alone or cocultured with MDSCs for 3 days. **O,P,** Flow cytometry analysis of SA-β-gal and p21 expression at indicated time points in $CD8^+$ T cells derived from naïve cells pretreated with the Foxo1 inhibitor AS1842856 (5μM, **O**) or the AMPK inhibitor Compound C (5μM, **P**), followed by culture alone or coculture with MDSCs for 3 days (n = 3-4 independent experiments). Data are presented as mean ± s.d. P values for enrichment analyses in A,B were adjusted using the Benjamini–Hochberg procedure; data in D,E,F,G,O,P were analyzed using two-way ANOVA followed by Šídák's multiple-comparisons test. *P < 0.05, **P < 0.01, ***P < 0.001, ****P < 0.0001; ns, not significant.

Figure 6

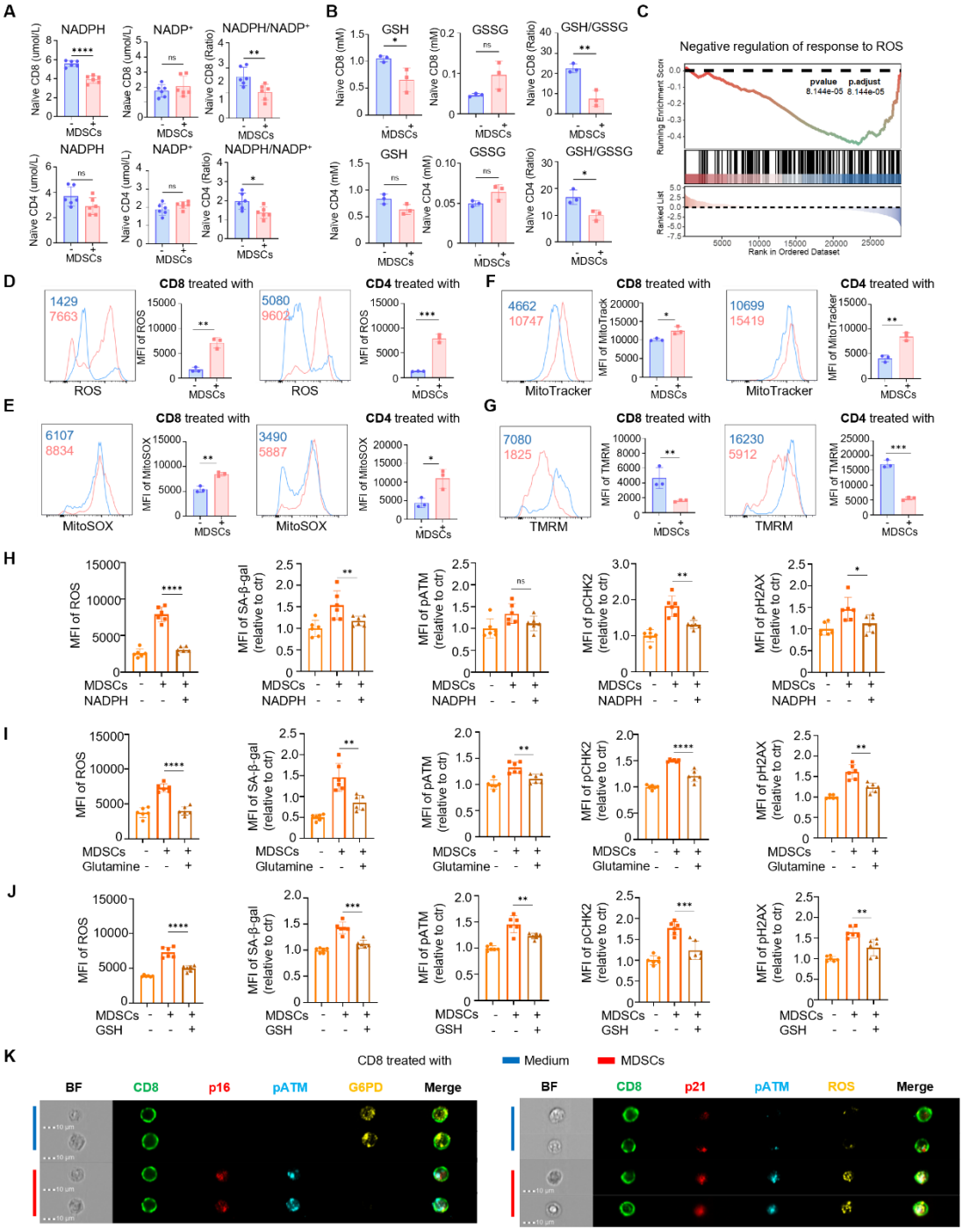


Fig. 6. MDSC-imposed metabolic restriction mediates T cell senescence by disrupting NADPH-dependent redox homeostasis. A, Quantification of NADPH and NADP$^+$ levels and the NADPH/NADP$^+$ ratio in CD8$^+$ and CD4$^+$ T cells derived from naïve cells cultured alone or cocultured with MDSCs for 3 days (n = 6 independent experiments). **B,** Quantification of GSH and GSSG levels and the GSH/GSSG ratio in CD4$^+$ and CD8$^+$ T cells derived from naïve cells cultured alone or cocultured with MDSCs for 3 days (n = 3 independent experiments). **C,** GSEA of ROS-regulated gene sets in CD8$^+$ T cells derived from naïve cells cocultured with MDSCs

for 3 days. **D-G,** Flow cytometry analysis of total ROS (**D**), mitochondrial ROS (MitoSOX; **E**), mitochondrial mass (MitoTracker; **F**), and mitochondrial membrane potential (TMRM; **G**) in $CD8^+$ and $CD4^+$ T cells derived from naïve cells cultured alone or cocultured with MDSCs for 3 days (n = 3 independent experiments). **H,** Flow cytometry analysis of ROS, SA-β-gal, and DNA damage-related molecules in $CD8^+$ T cells from naïve cells cocultured with MDSCs following exogenous NADPH supplementation (500 μM) (n = 6 independent experiments). **I,** Flow cytometry analysis of ROS, SA-β-gal, and DNA damage-related molecules in $CD8^+$ T cells from naïve cells cocultured with MDSCs following exogenous glutamine supplementation (2 mM) (n = 6 independent experiments). **J,** Flow cytometry analysis of ROS, SA-β-gal, and DNA damage-related molecules in $CD8^+$ T cells from naïve cells cocultured with MDSCs following exogenous GSH supplementation (500 μM) (n = 6 independent experiments). **K,** Imaging flow cytometry analysis of p-ATM colocalization with G6PD or ROS, and with p16 or p21 in $CD8^+$ T cells derived from naïve cells cultured alone or cocultured with MDSCs for 3 days. Data are presented as mean ± s.d. P values for GSEA in C were adjusted using the Benjamini–Hochberg procedure; data in A,B,D–G were analyzed using an unpaired two-tailed Student's t-test, and data in H–J using one-way ANOVA followed by Dunnett's multiple-comparisons test. *P < 0.05, **P < 0.01, ***P < 0.001, ****P < 0.0001; ns, not significant.

Figure 7

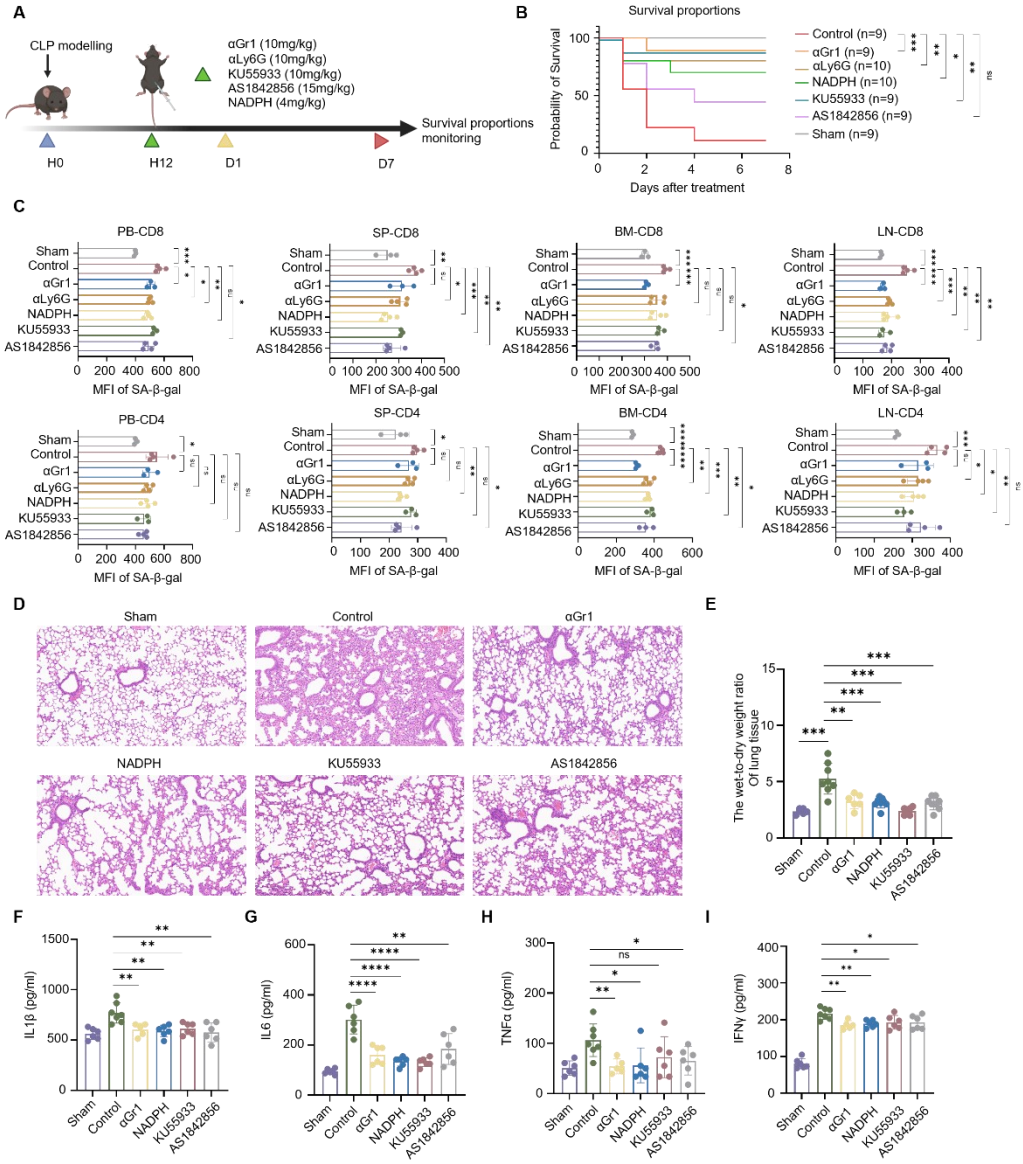


Fig. 7. Depletion of Gr1$^+$/Ly6G$^+$myeloid cells and systemic pharmacological interventions targeting ROS-DNA damage pathways alleviate systemic inflammation and organ injury and improve survival in septic mice. A, Schematic diagram of CLP-induced sepsis model establishment and *in vivo* intervention workflow. **B,** Kaplan-Meier survival curves for each group over 7 consecutive days (Sham, sham surgery group; Control, PBS-treated group; anti-Gr1, anti-Ly6G, NADPH, KU55933, and AS1842856, intervention groups; n = 9 mice per group, except anti-Ly6G and NADPH, n = 10). **C**, SA-β-gal staining of T cells from peripheral blood and multiple immune tissues 24 h after intervention in the Sham, Control (PBS-treated CLP), anti-Gr1, anti-Ly6G, NADPH, KU55933, and AS1842856 groups (n = 3–4 mice per group). **D,E,** Histological analysis of lung tissue by H&E staining (**D**) and quantification of lung wet/dry weight ratio (**E**) 24 h after intervention (n = 6-8 mice per group). **F-I,** Serum levels

of IL-1β (**F**), IL-6 (**G**), TNF-α (**H**), and IFN-γ (**I**) measured by ELISA 24 h after intervention (n = 5-7 mice per group). The groups analyzed in D–I included Sham, Control (PBS-treated CLP), anti-Gr1, NADPH, KU55933, and AS1842856. Survival curves in B were analyzed using the log-rank (Mantel–Cox) test. Data in C were analyzed using two-way repeated-measures ANOVA followed by Šídák's multiple-comparisons test. Data in E–I were analyzed using one-way ANOVA followed by Dunnett's multiple-comparisons test. Data are presented as mean ± s.d. *P < 0.05, **P < 0.01, ***P < 0.001, ****P < 0.0001; ns, not significant.

Figure 8

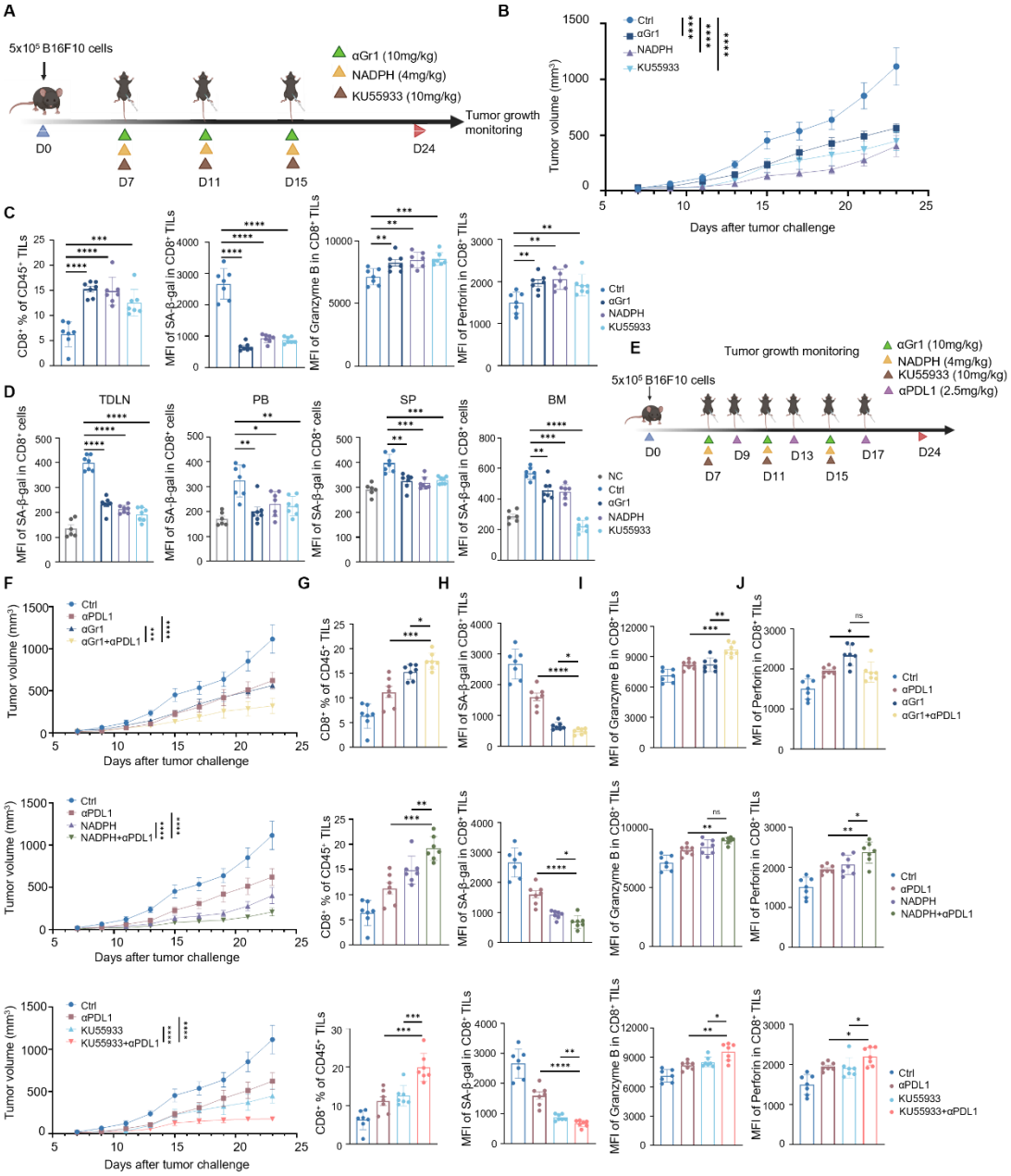


Fig. 8. Alleviating MDSC-mediated CD8⁺ T cell senescence enhances the antitumor efficacy of PD-L1 blockade in the B16F10 melanoma model. A, Schematic diagram of the experimental workflow for establishment of the B16F10 melanoma model and administration of intervention therapies (anti-Gr1, KU55933, or NADPH). **B,** Tumor growth curves over 24 days in mice from different treatment groups (Ctrl, PBS-treated control group; anti-Gr1, NADPH, and KU55933, intervention groups; n = 7 mice per group). **C,** Flow cytometry analysis of CD8⁺ T cell frequency, SA-β-gal activity, granzyme B, and perforin expression in tumor-infiltrating lymphocytes (n = 7 mice per group). **D,** Flow cytometry analysis of SA-β-gal expression in CD8⁺ T cells from peripheral blood and multiple immune tissues. TDLN,

tumor-draining lymph node; PB, peripheral blood; SP, spleen; BM, bone marrow. NC, normal control group; Ctrl, PBS-treated control group; anti-Gr1, NADPH, and KU55933, intervention groups (n = 6 mice for NC group; n = 7 mice for other groups). **E,** Schematic diagram of the experimental workflow for establishment of the B16F10 melanoma model and administration of combination therapy. **F,** Tumor growth curves over 24 days in mice from different treatment groups (Ctrl, PBS-treated control group; anti-PD-L1, anti-Gr1, anti-Gr1 plus anti-PD-L1, NADPH, NADPH plus anti-PD-L1, KU55933, and KU55933 plus anti-PD-L1, intervention groups; n = 7 mice per group). **G-J,** Flow cytometry analysis of $CD8^+$ T cell frequency (**G**), SA-β-gal activity (**H**), granzyme B expression (**I**), and perforin expression (**J**) in tumor-infiltrating lymphocytes (n = 7 mice per group). Bar charts are presented as mean ± s.d. Tumor growth curves are presented as mean ± s.e.m. Tumor-growth curves in B,F were analyzed using two-way repeated-measures ANOVA followed by Šídák's multiple-comparisons test; data in C were analyzed using one-way ANOVA followed by Dunnett's test, data in D using two-way repeated-measures ANOVA followed by Šídák's test, and data in G–J using one-way ANOVA followed by Tukey's multiple-comparisons test. *P < 0.05, **P < 0.01, ***P < 0.001, ****P < 0.0001; ns, not significant.